Interestingly, other reports have shown Cv2 to have an anti-BMP role in various in vitro and in vivo contexts (Ambrosio et al., 2008; Binnerts et al., 2004; Coles et al., 2004; Harada et al., 2008; Kelley et al., 2009; Moser et al., 2003; Rentzsch et al., 2006; Zhang et al., 2007, 2008). For instance, Cv2 exerts both pro- and anti-BMP activities when injected into the zebrafish embryo (Rentzsch et al., 2006). In the *Xenopus* gastrula, Cv2 acts predominantly as an anti-BMP factor (Ambrosio et al., 2008). While endocytic internalization is proposed to contribute to Cv2's anti-BMP activity, this machinery appears to be restricted to a limited range of cell types (Kelley et al., 2009). Biochemical and crystal structure analyses suggest that vertebrate Cv2 may interfere with BMP ligand-receptor binding via its Chordin-type cysteine-rich domain (CR1; Zhang et al., 2007; Zhang et al., 2008), although the in vivo relevance of such molecular interactions remains elusive. More recently, Cv2 was shown to bind other proteins, such as Chordin (Ambrosio et al., 2008), suggesting that Cv2's function is complex, and its role as a pro- or anti-BMP factor may be context-dependent. Therefore, careful investigation is required to identify the in vivo role of Cv2 in different developmental contexts.

Previously, by showing a genetic enhancement between *Bmp4* and *Cv2*, we demonstrated that Cv2 functions as a pro-BMP factor in vertebral and eye development (Ikeya et al., 2006). In the same study, we found kidney defects (hypoplasia) in *Cv2*-null mouse embryos. Our previous report showed that Cv2 acts in the same direction with Kcp, which functions as a pro-BMP factor in a different context (Ikeya et al., 2006; Lin et al., 2005). However, our previous study could not tell whether Cv2 in the developing kidney was required as a pro- or anti-Bmp factor, because of the lack of genetic evidences showing functional interaction between Cv2 and Bmp ligands.

Here, we report that Cv2 plays an essential role as a pro-BMP factor in mouse kidney development. We found that Cv2 promotes the BMP-dependent formation of the cap condensates, and we present genetic evidence that the pro-BMP function of Cv2 is dependent on the presence of Tsg, another BMP modulator. These results demonstrate that an extracellular system for modulating local BMP signals via Cv2 and Tsg plays a key role in the early steps of mouse nephron development.

Materials and methods

Mutant mice and crosses

Mice carrying mutations in *Cv2*, *Bmp7*, *Tsg*, and *Smad1* were described previously (Hayashi et al., 2002; Ikeya et al., 2006; Luo et al., 1995; Nosaka et al., 2003). We crossed $Cv2^{+/-}$ mice with $Bmp7^{+/-}$, $Tsg^{-/-}$ or $Smad1^{+/-}$ mice to obtain compound heterozygotes. No obvious defects were observed in the compound heterozygotes, and we used them for further intercrosses. Genotypes were confirmed by PCR (Ikeya et al., 2006, 2008). Animals were housed in environmentally controlled rooms in accordance with RIKEN guidelines for animal experiments.

LacZ staining, histology, immunohistochemistry, and statistics

LacZ staining, histology, and immunohistochemistry were performed as described previously (Ikeya et al., 2006). Primary antibodies and dilutions were as follows: anti-alpha-catenin, 1:500 (Sigma, rabbit polyclonal); anti-BF2, 1:500 (Abcam, goat polyclonal); anti-cadherin-11, 1:500 (R&D, goat polyclonal); anti-Cv2, 1:1000 (R&D, goat polyclonal); anti-E-cadherin, 1:500 (Takara, ECCD2); anti-β-galactosidase, 1:5000 (Cappel, rabbit polyclonal) or 1:2000 (AbD Serotec, goat polyclonal); anti-laminin, 1:500 (Chemicon, AL-4); anti-NCAM, 1:1000 (Chemicon, rabbit polyclonal); anti-Pax2, 1:200 (Zymed, rabbit polyclonal); anti-phospho-Smad1/5/8, 1:30 (Cell Signaling, rabbit polyclonal); and anti-WT1, 1:50 (Santa Cruz, rabbit polyclonal). For staining with the anti-WT1 antibody, citrate buffer, pH 6, was used for antigen retrieval (Zymed) in a 2100 Retriever (PickCell Laboratories). The anti-Cv2 polyclonal antibody recognizes both N- and C-halves of cleaved Cv2 (data not shown).

The signal intensity of the phospho-Smad1/5/8 staining was compared as follows, using the ImageJ software (National Institutes of Health, Bethesda, MD). We stained sections with phospho-Smad1/5/8-specific antibody and DAPI and acquired images by scanning the sections with a confocal microscope (LSM510 (Zeiss)). The images were trimmed into smaller ones showing either cap condensates or collecting ducts, and we divided the total signal intensity of phospho-Smad1/5/8 in the trimmed regions by DAPI-positive area. We defined this value as the "average signal intensity" of phospho-Smad1/5/8 and compared it across images. No differences were observed among the average signal intensities of the collecting ducts, regardless of the genotype. We regarded average signal intensities from cap condensates that were less than two thirds of the collecting duct average intensity as "reduced."

The numbers of nephrons and nephron progenitors at E18.5 were counted as described previously (Ikeya et al., 2006). We scored eight to 20 embryos of each genotype to obtain these numbers. The number of LacZ-positive cap condensates at E13.5, 14.5, and 15.5 was obtained from six to 30 kidneys from each genotype.

Statistical analyses were performed using GraphPad Prism 4 (GraphPad Software).

Cell culture, transfection, siRNA, and luciferase assay

HEK293T cells were maintained in DMEM/10% FCS (HyClone). To examine the effect of Cv2 on BMP signaling, reverse transfections were performed in a 24-well cell culture plate (BD Falcon) using FuGene6 (Roche, Basel, Switzerland) with a total of 210 ng DNA [100 ng of BRE-luc (Korchynskyi and ten Dijke, 2002), 10 ng of phRL-null (Promega), and the indicated dose of CIG-mCv2 and CIG-LacZ (Megason and McMahon, 2002)] per well, in DMEM/1% FCS. Annealed and purified siRNA duplexes were obtained from Ambion (Austin, TX) and were added at 75 ng per well 4 h prior to the cDNA transfection with X-treme Gene (Roche, Basel, Switzerland). After 16 h of treatment, the cells were lysed and assayed for luciferase activity using the dual luciferase reporter assay system (Promega, Madison, WI), according to the manufacturer's instructions.

Results

Enhancement of hypoplastic phenotypes in the $Cv2^{-/-}$ kidney by $Bmp7^{+/-}$ mutation

We previously demonstrated that *Cv2*-null mice display a reduced kidney size and lower nephron number than wild-type mice (Ikeya et al., 2006). To examine the role of Cv2 during nephrogenesis, we first analyzed *Cv2*'s expression patterns during kidney development in *nLacZ*-knock-in mice ($Cv2^{+/nLacZ}$). At E11.5, the metanephric blastema expressed $Cv2^{nLacZ}$, whereas the ureteric buds were negative for it (Figs. 1A–C). At E12.0, the maturating stromal cells located in the central portion of the kidney became $Cv2^{nLacZ}$-negative (asterisk in Fig. 1D). At E13.5 and E14.5, the $Cv2^{nLacZ}$ expression was mainly restricted to the cap condensates (Figs. 1E–H, and data not shown) and to portions of the forming nephrons (pretubular aggregates, comma-shaped body, and S-shaped body) and Bowman's capsules (Supplementary Figs. S1A–D). Immunohistochemical analyses confirmed that cap condensate cells positive for Pax2 strongly expressed $Cv2^{nLacZ}$, but the peripheral stroma, which was positive for BF2, and collecting ducts did not (Supplementary Figs. S2A–C). From E14 until birth, the $Cv2^{nLacZ}$ expression was restricted to the cap condensates and its derivatives (data not shown).

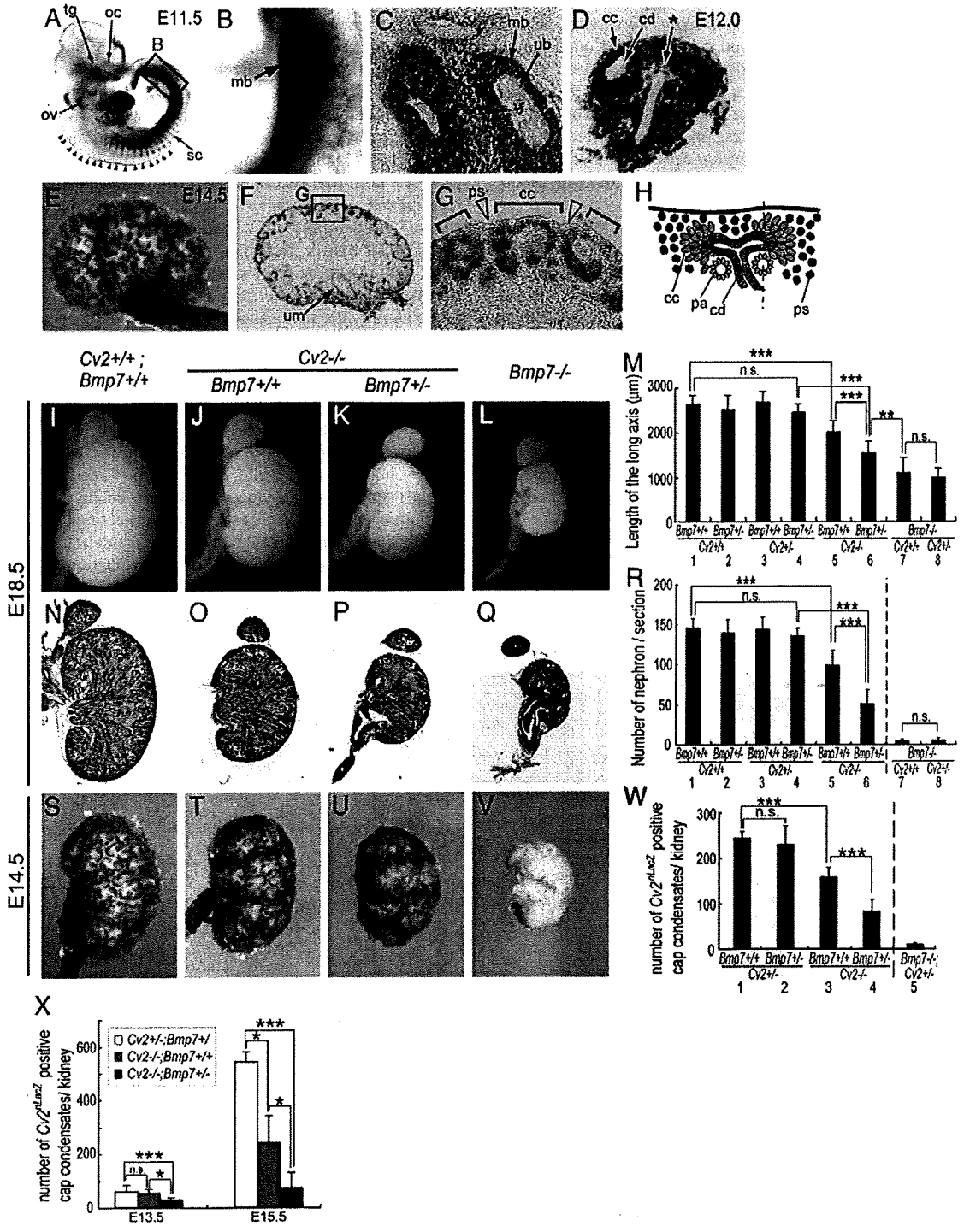

Fig. 1. Cooperative roles of *Cv2* and *Bmp7* in kidney development. (A–G) Expression of *Cv2* analyzed with *nLacZ* knock-in mice. (A–C) At E11.5, LacZ staining was observed in the trigeminal ganglion (tg), optic cup (oc), otic vesicle (ov), sclerotome (sc), roof plate of the neural tube (triangles), and metanephric blastema (mb), but not in the ureteric bud (ub). (D) At E12.0, the central portion of the metanephric mesenchyme became $Cv2^{nLacZ}$ negative (asterisk). cd, collecting duct; cc, cap condensates. (E–G) At E14.5, $Cv2^{nLacZ}$ was preferentially expressed in the cap condensates (bracket in G) and the ureteric mesenchyme (um). Triangles in (G) indicate that the peripheral stroma (ps) was $Cv2^{nLacZ}$-negative. (H) Schematic representation of the cortical region of the embryonic kidney. pa, pretubular aggregate. (I–L) External appearances of the control, $Cv2^{-/-}$, $Bmp7^{+/-}$;$Cv2^{-/-}$, and $Bmp7^{-/-}$ kidneys at E18.5. (M) Length of the long axis. (N–Q) Longitudinal sections stained with hematoxylin and eosin at E18.5. (R) The number of nephrons in the maximal longitudinal sections. (S–V) External views at E14.5 stained with $Cv2^{nLacZ}$. (W, X) The number of $Cv2^{nLacZ}$-positive cap condensates at E14.5 (W, Tukey test), and E13.5 and E15.5 (X, Bonferroni test). Error bars show S.D.; n.s., no significant difference; ***$P<0.001$; **$P<0.01$; *$P<0.05$. In (R) and (W), statistical analyses of the $Bmp7^{-/-}$ samples were performed separately because of significant differences among the S.D.s.

Although these expression patterns, as well as the *Cv2*-null phenotypes, suggest a crucial role for Cv2 in nephrogenesis, the molecular mechanism of Cv2's action, and particularly whether it functioned as a pro-BMP or anti-BMP factor in this developmental context, was unclear. Among the *Bmp* genes, *Bmp7* is strongly expressed in the cap condensate, as well as in the ureteric bud, collecting duct, and forming nephron (Supplementary Fig. S3A; Dudley and Robertson, 1997; Godin et al., 1998), and its mutation causes progressive renal hypoplasia (Dudley et al., 1995; Luo et al., 1995). In addition, Cv2 binds BMP7 with a high affinity (Zhang et al., 2007). These findings suggested that Cv2 might interact with BMP7 in kidney development. We therefore tested their functional interaction by crossing *Cv2* mutants with *Bmp7* mutants (Figs. 1I–X).

At E18.5, the loss of one allele of *Bmp7* in the $Cv2^{+/+}$ or $Cv2^{+/-}$ background had no obvious effects on kidney development (Figs. 1M, R, lanes 1–4). Similarly, the loss of one *Cv2* allele in the $Bmp7^{-/-}$ background had little effect on kidney size or nephron number (Figs. 1M, R, lanes 7, 8). In contrast, the deletion of a single *Bmp7* allele in the $Cv2^{-/-}$ background caused further reductions in the kidney size and nephron number at E18.5 than seen in $Cv2^{-/-}$ mice at the same age (Figs. 1J, K, O, P; Figs. 1M, R, lanes 5, 6).

A similar genetically enhanced reduction in the number of cap condensates (marked by the expression of $Cv2^{nLacZ}$) was evident during the early stages of kidney development, even at E14.5 and E15.5 (Figs. 1S–X). In addition, the enhanced decrease in the components of the forming nephrons (comma- and S-shaped bodies) was obvious in the $Bmp7^{+/-}$;$Cv2^{-/-}$ kidney, particularly at E15.5 (Fig. 1X and Supplementary Fig. S4).

These observations support the idea that Cv2 plays a pro-BMP role in the early phases of nephron formation.

Cv2 is essential for high levels of BMP signaling in cap condensates

These findings prompted us to study the expression and functions of Cv2 proteins in the early embryonic kidney. To this end, we performed immunohistochemical analysis of Cv2 protein in the developing kidney (Fig. 2). At E12.5 and E14.5, the Cv2 protein had accumulated in two regions: the pericellular region of the $Cv2^{nLacZ}$-expressing cap condensates (punctate signals; arrows in Figs. 2G–I) and the basement membrane of the collecting ducts (continuous signals; arrowheads in Figs. 2B, E). No immunostaining was observed in the $Cv2^{-/-}$ kidney, demonstrating the specificity of the antibody (Fig. 2F). Both the pericellular and the basement membrane signals co-localized with fibronectin (Figs. 2G–I) and laminin (data not shown), suggesting that Cv2 protein is densely accumulated in the extracellular matrix. This finding is in accordance with the previous work demonstrating Cv2's co-localization with extracellular matrix (Rentzsch et al., 2006; Serpe et al., 2008).

To identify the site of action of Cv2 in renal development, we next analyzed the levels of intracellular BMP signaling in wild-type and mutant mice by detecting a downstream component of BMP signaling, phosphorylated Smad1/5/8 (pSmad1), which is frequently used to assay BMP activity. At E14.5, high pSmad1 signals were observed in both the cap condensates (cc) and the tips of the collecting ducts (cd) in wild-type and $Bmp7^{+/-}$ embryos (Fig. 3A and Supplementary Fig. S5). In contrast, in $Cv2^{-/-}$, $Bmp7^{+/-}$;$Cv2^{-/-}$, and $Bmp7^{-/-}$ embryos, pSmad1 staining was reduced in the cap condensates, whereas no substantial change was observed in the collecting ducts (Figs. 3B–D). Fig. 3I shows the percentages of cap condensates with reduced pSmad1 signals (in this analysis, signal levels comparable to those in the collecting duct cells were considered to be high). As shown

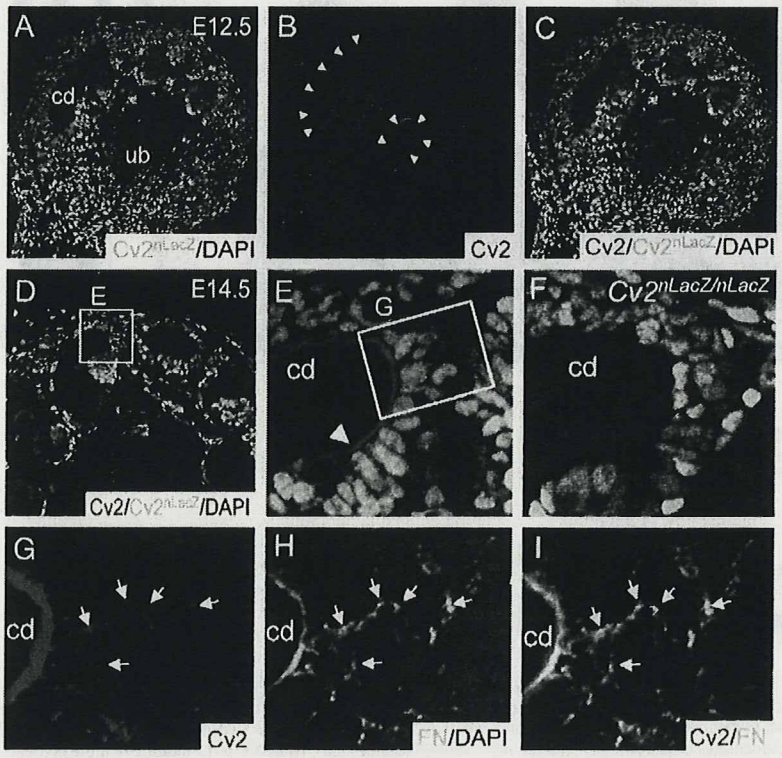

Fig. 2. Distribution of the Cv2 protein. Cv2 protein was accumulated in both the pericellular region of the cap condensate and the basement membrane of the collecting duct. (A–C) Immunohistochemistry with anti-Cv2 antibody at E12.5. Arrowheads, accumulation of Cv2 on the surface of the collecting duct and ureteric bud. (D–I) At E14.5, anti-Cv2 staining was observed in the pericellular region of the $Cv2^{nLacZ}$-positive cells (arrows in G–I) and the basement membrane of the collecting duct (arrowhead in E). (F) No signal was detected in the $Cv2^{-/-}$ mutants. Punctate pericellular signals co-localized with fibronectin (FN; arrows in G–I).

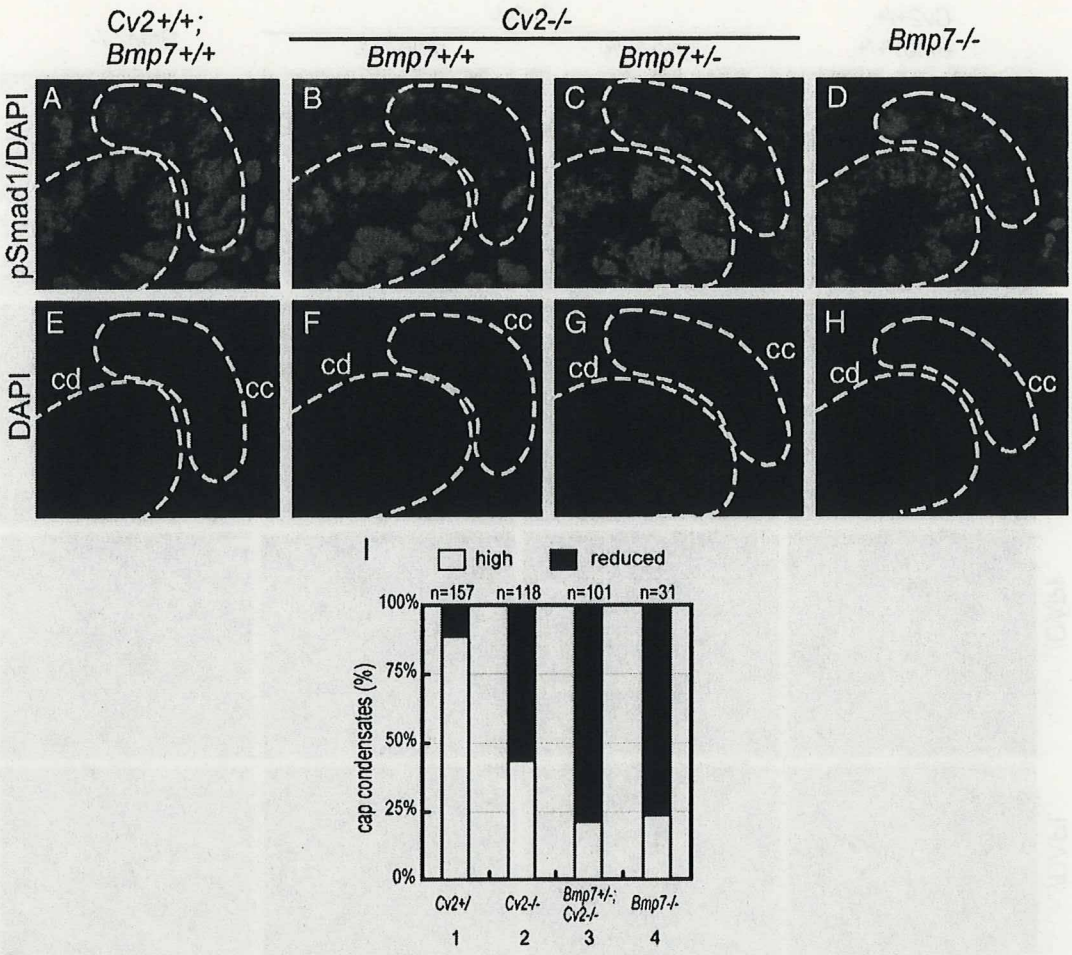

Fig. 3. A pro-BMP role of *Cv2* in the cap condensates but not in the collecting ducts. Staining intensity of pSmad1 was decreased in cap condensates of $Cv2^{-/-}$, $Bmp7^{+/-};Cv2^{-/-}$, and $Bmp7^{-/-}$ kidneys, but it was unchanged in the collecting ducts from all genotypes. Blue, DAPI; red, phospho-Smad1/5/8 (pSmad1)-specific antibody. (I) Percentages of cap condensates showing reduced pSmad1 signal intensity. Under the $Cv2^{-/-}$ background, the $Bmp7^{+/+}$ and $Bmp7^{+/-}$ groups exhibited a significant differences (P value = 0.0007) by Chi-square test.

(Fig. 3I, lanes 2 and 3), the additional deletion of one *Bmp7* allele enhanced the reduction of pSmad1 in the $Cv2^{-/-}$ background, suggesting that Cv2 acts in the same direction as BMP7 (i.e., as a pro-BMP factor).

These observations indicate that Cv2 is essential for enhancing BMP signals in the cap condensate during kidney organogenesis, but that the high BMP signals in the collecting ducts are independent of Cv2, suggesting a tissue-specific mode of Cv2's action.

Incomplete cellular aggregation in the $Cv2^{-/-}$ cap condensates

During nephrogenesis, cap condensates are formed as compact cell aggregates at the tips of the collecting ducts (cc in Fig. 4A). As shown above, BMP signaling was attenuated in the cap condensates of $Cv2^{-/-}$ and $Bmp7^{+/-};Cv2^{-/-}$ mutants. In addition, thin section analysis revealed impaired cell–cell attachment in the $Cv2^{-/-}$ and $Bmp7^{+/-};Cv2^{-/-}$ cap condensates (see loosely packed aggregates in Figs. 4B, C; E14.5), although the cells looked healthy and did not exhibit signs of apoptosis such as picnosis. These observations indicate that the loss of Cv2's pro-BMP function not only reduced the cap condensate number but also caused abnormal cellular aggregation.

Next, we further examined the cellular aggregation by immunostaining. While adhesion molecules such as NCAM and cadherin11 (also alpha-catenin) were distributed uniformly in the cell–cell interface regions in the cap condensate of control embryos (Figs. 4E, I, M), these protein appeared discontinuous or punctate in the $Cv2^{-/-}$ and $Bmp7^{+/-};Cv2^{-/-}$ mutants (arrowheads in Figs. 4F, G, J, K, N, O). These changes did not seem to be caused by a loss of specific cell types, since the cell type-specific markers (Pax2 and p75 for the cap condensate and BF2 for the peripheral stroma) were expressed normally in these mice (Figs. 4Q–S, and data not shown). Rather, these results indicate that a local augmentation of BMP signaling by Cv2 is crucial for the proper formation of cap condensates, including the cap–cell aggregation, during kidney development.

To focus in on which developmental step was most dependent on Cv2, we investigated the marker expression and aggregation of the cap cells in the $Bmp7^{-/-}$ kidney. We found, as reported previously, that the number of $Pax2^{+}$ cells in the $Bmp7^{-/-}$ cap condensates was severely reduced (Fig. 4T; Dudley et al., 1995; Luo et al., 1995). The adhesion molecules were found in a discontinuous pattern (Figs. 4H, L, P), resembling those in the *Cv2* mutants. In addition, the morphology of $Bmp7^{-/-}$ cap condensates were substantially impaired (even more drastically than $Cv2^{-/-}$ and $Bmp7^{+/-};Cv2^{-/-}$ condensates), consisting of cells with a generally round shape (Fig. 4D). These results imply that the complete loss of BMP7 signaling affected the cap condensate in terms of both the cellular presence (Pax2 expression; as reported previously (Dudley et al., 1995; Dudley and Robertson, 1997; Luo et al., 1995)) and the formation of the aggregates. In contrast, the

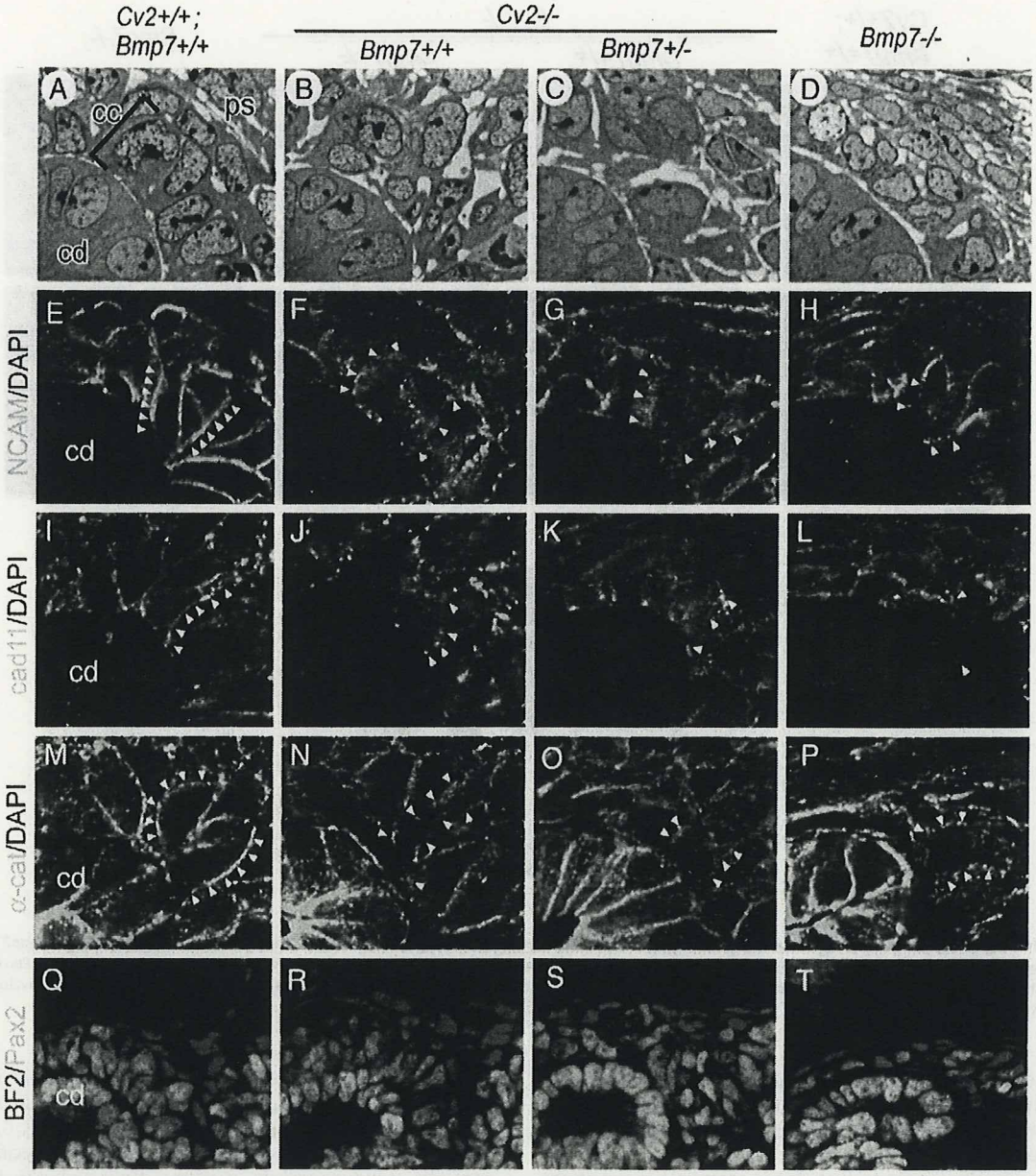

Fig. 4. Cv2 required for the cellular aggregation of the cap condensates. (A–D) Plastic thin sections stained with toluidine blue. In *Cv2*$^{-/-}$ and *Bmp7*$^{+/-}$;*Cv2*$^{-/-}$ kidneys, cap condensate cells adhered loosely to one another. In the *Bmp7*$^{-/-}$ kidney, the cells on the tip of the collecting duct became round. (E–P) Disturbed distribution of adhesion proteins in the cap condensates of the mutants. Immunohistochemistry with (E–H) anti-NCAM, (I–L) anti-cadherin11, and (M–P) anti-alpha-catenin. (Q–T) Immunohistochemistry with anti-Pax2 (green) and anti-BF2 (red). The Pax2-positive cap condensates and collecting ducts and the BF2-positive peripheral stroma developed normally in the *Cv2*$^{-/-}$ and *Bmp7*$^{+/-}$;*Cv2*$^{-/-}$ mutants. In the *Bmp7*$^{-/-}$ kidney, the number of Pax2-positive cells was markedly reduced.

attenuation of BMP signaling caused by the loss of Cv2 preferentially impaired the formation of the cellular aggregates.

Tsg mutation is epistatic to the Cv2 mutation in the kidney-defect phenotype

Taken together, our genetic and histochemical analyses demonstrated that Cv2 is an essential pro-BMP factor for the development of cap condensates in the early embryonic kidney. An obvious remaining question is how Cv2 promotes BMP signaling in these cells.

Very recently, two independent studies (from De Robertis' and our groups) reported a genetic interaction between *Cv2* and *Tsg* in skeletal development (Ikeya et al., 2008; Zakin et al., 2008). The major skeletal defects of the *Cv2*-null mutant mice (in the thoracic and lumbar vertebrae) are suppressed in *Tsg*$^{-/-}$;*Cv2*$^{-/-}$ embryos, which show moderate skeletal phenotypes (Nosaka et al., 2003; Petryk et al., 2004; Zakin and De Robertis, 2004). This suggests that the *Tsg* mutation is epistatic to the *Cv2* mutation in skeletal development. However, the precise molecular and cellular mechanism of this gene interaction in embryonic development was still unknown.

With this in mind, we examined possible interactions between *Cv2* and *Tsg* in kidney development (*Tsg* expression is detected diffusely in the developing kidney (Supplementary Fig. S3B; Nosaka et al., 2003)). In nephrogenesis, as opposed to skeletal development, interactions with the *Tsg* mutation can be analyzed rather simply, because the *Tsg* mutation itself does not cause significant embryonic kidney

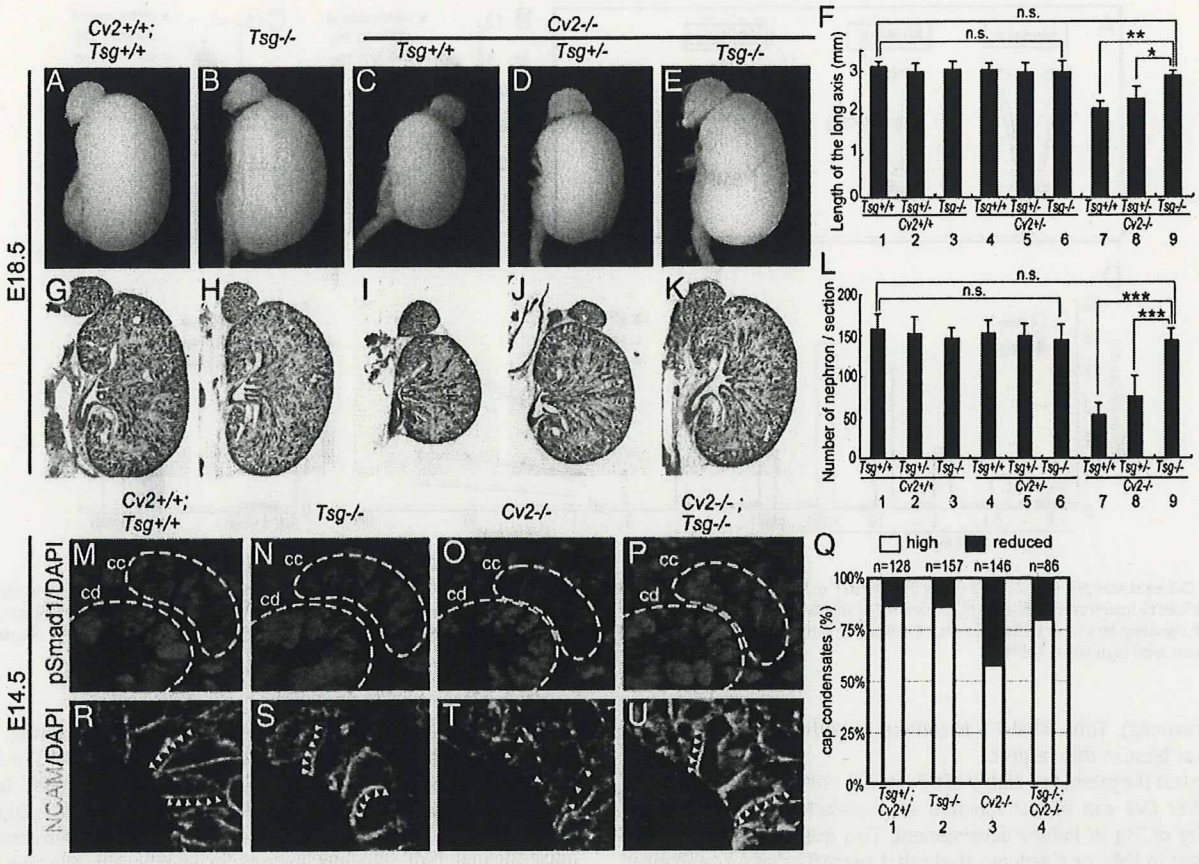

Fig. 5. Evidence for a *Tsg*-dependent pro-BMP function of *Cv2* in vivo. Renal phenotypes of $Cv2^{-/-}$ rescued by the deletion of both alleles of *Tsg* at E18.5 and E14.5. (A–E) External views at E18.5. (F) Length of the long axis. (G–K) Histological sections at E18.5. (L) The number of nephrons in the maximal longitudinal sections. (M–P) Immunohistochemistry with anti-pSmad1 at E14.5. (Q) Percentages of cap condensates exhibiting reduced pSmad1 signal intensity. (R–U) Immunohistochemistry with anti-NCAM at E14.5. Error bars show S.D.; n.s., no significant difference; ***$P<0.001$; **$P<0.01$; *$P<0.05$ (Bonferroni test).

phenotypes (Nosaka et al., 2003). In the $Cv2^{+/+}$ and $Cv2^{+/-}$ backgrounds, the loss of both *Tsg* alleles did not significantly affect kidney size or nephron number at E18.5 (Figs. 5A, B, G, H; Figs. 5F, L, lanes 1–6). In contrast, when combined with the $Cv2^{-/-}$ mutation, the elimination of *Tsg* completely suppressed the renal defects otherwise present in *Cv2*-null mutants (Figs. 5C–E, I–K; Figs. 5F, L, lanes 1, 7–9). The *Tsg* deletion also restored the levels of BMP signaling (reduced pSmad1 levels) in the cap condensates of *Cv2*-null mutants at E14.5 (Figs. 5M–Q) and rescued the impaired cell–cell adhesion in the condensates (Figs. 5R–U).

These in vivo findings suggest a unidirectional dependence in which the pro-BMP function of Tsg requires Cv2, while Cv2 function is not dependent on Tsg activity.

Tsg-dependent mechanism of Cv2's pro-BMP function in cultured embryonic kidney cells

The suppression of the $Cv2^{-/-}$ kidney phenotypes by the *Tsg* mutation implied that, as a whole, Cv2 and Tsg act in opposite directions. That is, they appeared to play pro-BMP and anti-BMP roles, respectively, during nephrogenesis. Interestingly, previous studies suggested that Tsg can act as an anti-BMP or pro-BMP factor, depending on the context (Chang et al., 2001; Harland, 2001; Larrain et al., 2001; Oelgeschlager et al., 2000; Ross et al., 2001; Scott et al., 2001). For instance, genetic interaction studies of mouse *Tsg*-null mutations with *Bmp4* and *Bmp7* mutations show *Tsg* acting as a pro-BMP factor in head development and posterior mesodermal patterning (Zakin and De Robertis, 2004; Zakin et al., 2005). In *Xenopus* embryos, the Chordin–Tsg complex binds to BMPs and inhibits their signaling more efficiently than Chordin, an anti-BMP factor, does alone (anti-BMP activity of Tsg; Oelgeschlager et al., 2000; Scott et al., 2001). In the presence of the Chordin-degrading enzyme Xolloid, on the other hand, Tsg dislodges BMP from cleaved Chordin fragments, resulting in enhanced BMP signaling (a pro-BMP activity; Oelgeschlager et al., 2000).

Given the context-dependent bidirectional functions of Tsg and our findings in this study, the following hypothetical models could explain the functional interaction between Cv2 and Tsg in nephrogenesis. (1) The pro-BMP factor Cv2 and the anti-BMP factor Tsg act independently on BMP signals as simple antagonists (Fig. 6A, Model a). (2) Cv2 acts as a pro-BMP factor by interfering with the anti-BMP function of Tsg (Fig. 6A, Model b). (3) Tsg has simultaneous dual functions as both a pro-BMP and an anti-BMP factor, while Cv2 acts as a co-factor to strengthen the pro-BMP aspect of Tsg's functions (Fig. 6A, Model c).

Given that the fine-tuning of BMP signals is vital for kidney organogenesis (Cain et al., 2008), the phenotypical discrepancy between the normal kidney development of $Tsg^{-/-}$ embryos and the marked hypoplasia of *Cv2*-null embryos is rather difficult to explain with hypothetical Models a and b, which predict hyperactive BMP levels in $Tsg^{-/-}$ kidneys. In contrast, the BMP activity level under the $Tsg^{-/-}$ condition would be less affected in the hypothetical Model c, in which the simultaneous loss of both the anti- and pro-BMP functions could reduce the extent of change in signaling strength (Supplementary Fig. S6B). Consistent with this idea, we have not seen substantial changes in pSmad1 levels in $Tsg^{-/-}$ embryonic kidneys compared with control kidneys (Fig. 5N and our preliminary

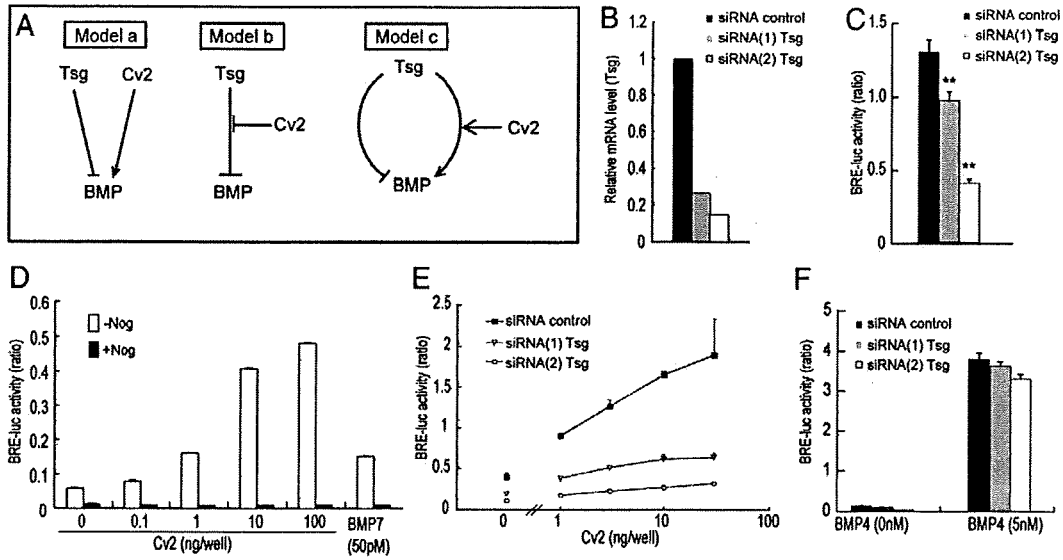

Fig. 6. Cv2 enhances pro-BMP activity of Tsg in HEK293T cell. (A) Models of the interaction between Tsg and Cv2. (B) Knockdown efficiency of Tsg mRNA. Expression levels were determined by quantitative real-time PCR analysis. (C) siRNA targeting of *Tsg* attenuates BMP signaling. Error bars show S.D.; $^{**}P<0.01$ (Dunnet test). (D) Dose-dependent activation of BMP signaling by *Cv2* in HEK293T cells. (E) siRNA targeting of *Tsg* reduces dose-dependent activation of BMP signaling by *Cv2*. (F) *Tsg* knockdown cells respond normally to treatment with high levels BMP4.

observations). Thus, Model c is consistent with the in vivo phenotype, at least in this respect.

To test the predictive ability of this model, one essential question is whether Cv2 can in fact function as a co-factor for the pro-BMP activity of Tsg in kidney development. This question is particularly relevant in light of a *Xenopus* study that suggests that Cv2 enhances the anti-BMP activity of Tsg in a different developmental context (dorsal-ventral patterning during gastrulation) (Ambrosio et al., 2008). Therefore, we next examined whether Cv2 promotes BMP signaling under the condition in which Tsg predominantly exerts a pro-BMP activity over an anti-BMP function.

In a series of preliminary experiments, we found that a human embryonic kidney-derived cell line, HEK293T, expresses *Tsg* as well as *Cv2* and *BMPs* (Supplementary Fig. S7), and that endogenous Tsg acted predominantly as a pro-BMP factor, since, when Tsg was knocked down by siRNAs (see Fig. 6B for the knockdown efficiency), the BMP signaling reporter (*BRE-luc*) activity was reduced accordingly (Fig. 6C). In this cell line, the expression of exogenous *Cv2* (introduced by plasmid transfection) strongly augmented the BMP signal in a dose-dependent manner, showing a pro-BMP activity (Fig. 6D, open columns). This augmentation appeared to depend on extracellular BMP signaling, since the addition of Noggin to the culture medium completely suppressed it (Fig. 6D, closed columns). Importantly, there was little augmentation of BMP signaling by *Cv2* in the *Tsg*-depleted HEK293T cells (Fig. 6E). This absence of the *Cv2*-induced increase in the *Tsg*-depleted cells was not owing to a general loss of the cellular BMP signaling pathway, because the *BRE-luc* activity was strongly stimulated by high concentrations of BMP4 also in these cells (Fig. 6F).

These data show that Cv2 functions as a pro-BMP factor in the presence of Tsg, which has a pro-BMP role in this embryonic kidney cell line, supporting the idea that Cv2 can enhance the pro-BMP activity of Tsg at least under certain situations (Fig. 6A, Model c).

Discussion

In this report, we demonstrated that Cv2 plays an essential pro-BMP role in early nephrogenesis. The cap condensate is the embryonic kidney tissue that normally expresses Cv2, and its development was substantially affected by the *Cv2*-null mutation, even during very early histogenesis. The loss of Cv2 directly attenuated the BMP signaling in this tissue, as assessed by its reduced pSmad1 levels (Fig. 3; in contrast, pSmad2 levels were largely unaffected; Supplementary Fig. S8). In contrast, the *Cv2* mutation did not substantially affect the high BMP signaling levels in the neighboring collecting duct cells, which do not normally express Cv2. Taken together, these observations suggest that Cv2 is a local (or short-range) enhancer of BMP signaling that mainly acts in a tissue-autonomous fashion. In other words, the tissue augments its own BMP response by expressing Cv2.

At least three mechanistic explanations for the context-dependent pro-BMP function of Cv2 have been advocated so far: (1) a cleaved Cv2 protein, rather than a full-length one, exerts a pro-BMP activity (shown in a zebrafish study; Rentzsch et al., 2006). (2) Cv2 is a biphasic BMP modulator acting in a dose-dependent manner that, only at a low dose, facilitates the binding of BMPs to their type I receptor (shown in a *Drosophila* study; Serpe et al., 2008). (3) Cv2 increases the local concentration of diffusible Chordin/Tsg/BMP protein complexes (e.g., on the ventral side in the case of the *Xenopus* embryo), which release active BMPs to their cell surface receptors upon the cleavage of Chordin by tolloid proteinases (proposed in a *Xenopus* study; Ambrosio et al., 2008). In this case, the entrapment of BMP into the complexes is an anti-BMP process, while the release of BMP from the accumulated Chordin/Tsg/BMP complexes (i.e., reservoir complexes for BMP) serves as a pro-BMP step.

Of the three proposals (which are not mutually exclusive), the last one (Mechanism 3) fits our in vivo and in vitro data particularly well. First, our immunostaining results showed that Cv2 proteins are associated with the pericellular matrix (Fig. 2), which could make Cv2 less diffusible. Since Cv2 can physically interact with Chordin, Tsg and BMP (Ambrosio et al., 2008), the Cv2-bound pericellular matrix supposedly contributes to the local accumulation of Chordin/Tsg/BMP complexes. Second, the *Cv2*-null mutation specifically affected the cap condensates, which are normally surrounded by auto/paracrine Cv2. Third, Cv2 functions as a pro-BMP factor in the presence of Tsg, which is evidence that Cv2 might function in a complex, as proposed for Mechanism 3.

In addition, Mechanism 3 appears to be compatible with Model c (Fig. 6A), in which pro- and anti-BMP functions of Tsg can co-exist. In this interpretation, which combines Model c and Mechanism 3, Cv2 preferentially enhances the pro-BMP activity of Tsg; this activity is expected to depend heavily on the Cv2-mediated local high concentration of reservoir complexes that potentially release BMP. In contrast, the inactivation of BMPs by their entrapment in the Chordin–Tsg complex (anti-BMP) is Cv2-independent presumably because the entrapment process itself does not require the specific localization of the complexes. By using an embryonic kidney cell line, in which the pro-BMP function of Tsg is predominantly observed (Fig. 6E), we presented the practical feasibility of Model c (Fig. 6A), at least with respect to the cooperative pro-BMP function of Cv2 and Tsg. Consistent with Model c and also Mechanism 3, Cv2 exerts pro-BMP function in the presence of Tsg in this cell culture system. In the future investigations, other models must also be ruled out, including one in which Cv2 acts as an inhibitor of Tsg's anti-BMP activity, rather than as a co-factor of its pro-BMP activity (a sort of fusion of Models b and c).

This report mainly focused on the pro-BMP role of Cv2. Genetic analyses of *Bmp7;Cv2* mutants provide firm evidences that Cv2 acts predominantly as a pro-BMP factor in early nephrogenesis. In addition, a genetic enhancement in the nephron number was observed between *Cv2* and *Smad1* (Supplementary Fig. S9), indicating that Cv2 works cooperatively not only with the extracellular BMP ligand (BMP7) but also with the major transducer of BMP receptor signaling. Although these data do not argue the presence of a minor anti-BMP function of Cv2, it is considered the total Cv2 activity, at least on balance, is deviated toward the pro-BMP direction in the context of kidney development.

This report also focused on its genetic interactions with Tsg. Whereas it is beyond the scope of this genetics-based study, identifying the detailed molecular mechanisms underlying the pro-BMP function at the protein level is an important topic for future comprehensive study (Umulis et al., 2009). For instance, it will be intriguing to show the different kinetics of BMP release from complexes of Cv2 with Tsg versus Cv2 with Chordin, or the concentration or presentation of the ligand-bearing complexes to the receptor. It is also interesting to learn whether the role of mammalian Tsg in kidney development in fact depends on Chordin, especially given that Chordin and Chordin-related genes are expressed in the embryonic kidney (Supplementary Fig. S10). Because good antibodies for immunohistochemical studies of Tsg, Chordin and the tolloids are not available (our preliminary observations), we cannot currently examine whether Tsg–Chordin complexes are concentrated or specifically degraded near the cap condensate. Visualizing the dynamic localization, diffusion and processing of the complex proteins is a challenging but critical future task.

Our preliminary study showed that the decrease of nephron numbers in $Cv2^{-/-}$ kidneys (E14.5) was also moderately enhanced by adding a $Bmp4^{+/-}$ mutation similar to that observed with $Bmp7^{+/-}$ mutation (Supplementary Fig. S11). On the other hand, during late nephrogenesis, the $Bmp4^{+/-}$ mutation strongly enhanced the hydroureter phenotypes in the $Cv2^{-/-}$ kidneys (Supplementary Fig. S12). In this case, the formation of the ureter mesenchyme, which expresses *Bmp4* but not *Bmp7*, was strongly inhibited, suggesting that BMP4 cooperates with Cv2 independently of BMP7, at least in this context. Thus, whether BMP7 acts as a homodimer or a heterodimer with BMP4 in the Cv2 interaction is a remaining question for further investigation.

Conclusion

From our in vivo and in vitro observations, we conclude that Cv2, in concert with Tsg, shapes the signaling landscape in the complex organogenetic microenvironment of the kidney, creating locally restricted peaks in the BMP signal.

Acknowledgments

We are grateful to the staff of the Laboratory of Animal Resources and Genetic Engineering at the Center for Developmental Biology for their help with mouse husbandry, and to Drs. H. Enomoto, M. Eiraku, H. Inomata, and A. Takai for invaluable comments and discussion. BRE-luc and CIG were kindly provided by Drs. P. ten Djike and A. McMahon, respectively. *Smad1* knockout mice were a kind gift of Dr. K Hayashi through Dr. M. Saitou. MI is thankful to Ayumi Ikeya and Yu-ichi Ikeya for constant encouragement and support during this study. This work was supported in part by grants-in-aid from the Ministry of Education, Culture, Sports, Science and Technology of Japan (Y.S. and M.I.), the Kobe Cluster Project, and the Leading Project (Y.S.), and by the Special Postdoctoral Researchers Program of RIKEN (M.I.).

Appendix A. Supplementary data

Supplementary data associated with this article can be found, in the online version, at doi:10.1016/j.ydbio.2009.11.013.

References

Ambrosio, A.L., Taelman, V.F., Lee, H.X., Metzinger, C.A., Coffinier, C., De Robertis, E.M., 2008. Crossveinless-2 Is a BMP feedback inhibitor that binds Chordin/BMP to regulate Xenopus embryonic patterning. Dev. Cell 15, 248–260.

Binnerts, M.E., Wen, X., Cante-Barrett, K., Bright, J., Chen, H.T., Asundi, V., Sattari, P., Tang, T., Boyle, B., Funk, W., Rupp, F., 2004. Human Crossveinless-2 is a novel inhibitor of bone morphogenetic proteins. Biochem. Biophys. Res. Commun. 315, 272–280.

Cain, J.E., Hartwig, S., Bertram, J.F., Rosenblum, N.D., 2008. Bone morphogenetic protein signaling in the developing kidney: present and future. Differentiation 76, 831–842.

Chang, C., Holtzman, D.A., Chau, S., Chickering, T., Woolf, E.A., Holmgren, L.M., Bodorova, J., Gearing, D.P., Holmes, W.E., Brivanlou, A.H., 2001. Twisted gastrulation can function as a BMP antagonist. Nature 410, 483–487.

Coles, E., Christiansen, J., Economou, A., Bronner-Fraser, M., Wilkinson, D.G., 2004. A vertebrate crossveinless 2 homologue modulates BMP activity and neural crest cell migration. Development 131, 5309–5317.

Conley, C.A., Silburn, R., Singer, M.A., Ralston, A., Rohwer-Nutter, D., Olson, D.J., Gelbart, W., Blair, S.S., 2000. Crossveinless 2 contains cysteine-rich domains and is required for high levels of BMP-like activity during the formation of the cross veins in Drosophila. Development 127, 3947–3959.

Dudley, A.T., Robertson, E.J., 1997. Overlapping expression domains of bone morphogenetic protein family members potentially account for limited tissue defects in BMP7 deficient embryos. Dev. Dyn. 208, 349–362.

Dudley, A.T., Lyons, K.M., Robertson, E.J., 1995. A requirement for bone morphogenetic protein-7 during development of the mammalian kidney and eye. Genes Dev. 9, 2795–2807.

Glinka, A., Wu, W., Onichtchouk, D., Blumenstock, C., Niehrs, C., 1997. Head induction by simultaneous repression of Bmp and Wnt signalling in Xenopus. Nature 389, 517–519.

Godin, R.E., Takaesu, N.T., Robertson, E.J., Dudley, A.T., 1998. Regulation of BMP7 expression during kidney development. Development 125, 3473–3482.

Harada, K., Ogai, A., Takahashi, T., Kitakaze, M., Matsubara, H., Oh, H., 2008. Crossveinless-2 controls bone morphogenetic protein signaling during early cardiomyocyte differentiation in P19 cells. J. Biol. Chem. 283, 26705–26713.

Harland, R.M., 2001. Developmental biology. A twist on embryonic signalling. Nature 410, 423–424.

Hayashi, K., Kobayashi, T., Umino, T., Goitsuka, R., Matsui, Y., Kitamura, D., 2002. SMAD1 signaling is critical for initial commitment of germ cell lineage from mouse epiblast. Mech. Dev. 118, 99–109.

Hemmati-Brivanlou, A., Kelly, O.G., Melton, D.A., 1994. Follistatin, an antagonist of activin, is expressed in the Spemann organizer and displays direct neuralizing activity. Cell 77, 283–295.

Hogan, B.L., 1996. Bone morphogenetic proteins: multifunctional regulators of vertebrate development. Genes Dev. 10, 1580–1594.

Hsu, D.R., Economides, A.N., Wang, X., Eimon, P.M., Harland, R.M., 1998. The Xenopus dorsalizing factor Gremlin identifies a novel family of secreted proteins that antagonize BMP activities. Mol. Cell 1, 673–683.

Ikeya, M., Kawada, M., Kiyonari, H., Sasai, N., Nakao, K., Furuta, Y., Sasai, Y., 2006. Essential pro-Bmp roles of crossveinless 2 in mouse organogenesis. Development 133, 4463–4473.

Ikeya, M., Nosaka, T., Fukushima, K., Kawada, M., Furuta, Y., Kitamura, T., Sasai, Y., 2008. Twisted gastrulation mutation suppresses skeletal defect phenotypes in Crossveinless 2 mutant mice. Mech. Dev. 125, 832–842.

Kamimura, M., Matsumoto, K., Koshiba-Takeuchi, K., Ogura, T., 2004. Vertebrate crossveinless 2 is secreted and acts as an extracellular modulator of the BMP signaling cascade. Dev. Dyn. 230, 434–445.
Kelley, R., Ren, R., Pi, X., Wu, Y., Moreno, I., Willis, M., Moser, M., Ross, M., Podkowa, M., Attisano, L., Patterson, C., 2009. A concentration-dependent endocytic trap and sink mechanism converts Bmper from an activator to an inhibitor of Bmp signaling. J. Cell Biol. 184, 597–609.
Kobayashi, A., Valerius, M.T., Mugford, J.W., Carroll, T.J., Self, M., Oliver, G., McMahon, A.P., 2008. Six2 defines and regulates a multipotent self-renewing nephron progenitor population throughout mammalian kidney development. Cell Stem Cell 3, 169–181.
Korchynskyi, O., ten Dijke, P., 2002. Identification and functional characterization of distinct critically important bone morphogenetic protein-specific response elements in the Id1 promoter. J. Biol. Chem. 277, 4883–4891.
Lamb, T.M., Knecht, A.K., Smith, W.C., Stachel, S.E., Economides, A.N., Stahl, N., Yancopolous, G.D., Harland, R.M., 1993. Neural induction by the secreted polypeptide noggin. Science 262, 713–718.
Larrain, J., Oelgeschlager, M., Ketpura, N.I., Reversade, B., Zakin, L., De Robertis, E.M., 2001. Proteolytic cleavage of Chordin as a switch for the dual activities of twisted gastrulation in BMP signaling. Development 128, 4439–4447.
Lin, J., Patel, S.R., Cheng, X., Cho, E.A., Levitan, I., Ullenbruch, M., Phan, S.H., Park, J.M., Dressler, G.R., 2005. Kielin/chordin-like protein, a novel enhancer of BMP signaling, attenuates renal fibrotic disease. Nat. Med. 11, 387–393.
Luo, G., Hofmann, C., Bronckers, A.L., Sohocki, M., Bradley, A., Karsenty, G., 1995. BMP-7 is an inducer of nephrogenesis, and is also required for eye development and skeletal patterning. Genes Dev. 9, 2808–2820.
Megason, S.G., McMahon, A.P., 2002. A mitogen gradient of dorsal midline Wnts organizes growth in the CNS. Development 129, 2087–2098.
Moser, M., Binder, O., Wu, Y., Aitsebaomo, J., Ren, R., Bode, C., Bautch, V.L., Conlon, F.L., Patterson, C., 2003. BMPER, a novel endothelial cell precursor-derived protein, antagonizes bone morphogenetic protein signaling and endothelial cell differentiation. Mol. Cell. Biol. 23, 5664–5679.
Moser, M., Yu, Q., Bode, C., Xiong, J.W., Patterson, C., 2007. BMPER is a conserved regulator of hematopoietic and vascular development in zebrafish. J. Mol. Cell. Cardiol. 43, 243–253.
Nosaka, T., Morita, S., Kitamura, H., Nakajima, H., Shibata, F., Morikawa, Y., Kataoka, Y., Ebihara, Y., Kawashima, T., Itoh, T., Ozaki, K., Senba, E., Tsuji, K., Makishima, F., Yoshida, N., Kitamura, T., 2003. Mammalian twisted gastrulation is essential for skeleto-lymphogenesis. Mol. Cell. Biol. 23, 2969–2980.
Oelgeschlager, M., Larrain, J., Geissert, D., De Robertis, E.M., 2000. The evolutionarily conserved BMP-binding protein twisted gastrulation promotes BMP signalling. Nature 405, 757–763.
Oxburgh, L., Chu, G.C., Michael, S.K., Robertson, E.J., 2004. TGFbeta superfamily signals are required for morphogenesis of the kidney mesenchyme progenitor population. Development 131, 4593–4605.
Petryk, A., Anderson, R.M., Jarcho, M.P., Leaf, I., Carlson, C.S., Klingensmith, J., Shawlot, W., O'Connor, M.B., 2004. The mammalian twisted gastrulation gene functions in foregut and craniofacial development. Dev. Biol. 267, 374–386.
Rentzsch, F., Zhang, J., Kramer, C., Sebald, W., Hammerschmidt, M., 2006. Crossveinless 2 is an essential positive feedback regulator of Bmp signaling during zebrafish gastrulation. Development 133, 801–811.
Ross, J.J., Shimmi, O., Vilmos, P., Petryk, A., Kim, H., Gaudenz, K., Hermanson, S., Ekker, S.C., O'Connor, M.B., Marsh, J.L., 2001. Twisted gastrulation is a conserved extracellular BMP antagonist. Nature 410, 479–483.
Sasai, Y., Lu, B., Steinbeisser, H., Geissert, D., Gont, L.K., De Robertis, E.M., 1994. Xenopus chordin: a novel dorsalizing factor activated by organizer-specific homeobox genes. Cell 79, 779–790.
Sasai, Y., Lu, B., Steinbeisser, H., De Robertis, E.M., 1995. Regulation of neural induction by the Chd and Bmp-4 antagonistic patterning signals in Xenopus. Nature 376, 333–336.
Scott, I.C., Blitz, I.L., Pappano, W.N., Maas, S.A., Cho, K.W., Greenspan, D.S., 2001. Homologues of twisted gastrulation are extracellular cofactors in antagonism of BMP signalling. Nature 410, 475–478.
Serpe, M., Umulis, D., Ralston, A., Chen, J., Olson, D.J., Avanesov, A., Othmer, H., O'Connor, M.B., Blair, S.S., 2008. The BMP-binding protein Crossveinless 2 is a short-range, concentration-dependent, biphasic modulator of BMP signaling in Drosophila. Dev. Cell 14, 940–953.
Shah, M.M., Sampogna, R.V., Sakurai, H., Bush, K.T., Nigam, S.K., 2004. Branching morphogenesis and kidney disease. Development 131, 1449–1462.
Simic, P., Vukicevic, S., 2005. Bone morphogenetic proteins in development and homeostasis of kidney. Cytokine Growth Factor Rev. 16, 299–308.
Smith, W.C., Harland, R.M., 1992. Expression cloning of noggin, a new dorsalizing factor localized to the Spemann organizer in Xenopus embryos. Cell 70, 829–840.
Umulis, D., O'Connor, M.B., Blair, S.S., 2009. The extracellular regulation of bone morphogenetic protein signaling. Development 136, 3715–3728.
Vainio, S., Lin, Y., 2002. Coordinating early kidney development: lessons from gene targeting. Nat. Rev. Genet. 3, 533–543.
Zakin, L., De Robertis, E.M., 2004. Inactivation of mouse twisted gastrulation reveals its role in promoting Bmp4 activity during forebrain development. Development 131, 413–424.
Zakin, L., Reversade, B., Kuroda, H., Lyons, K.M., De Robertis, E.M., 2005. Sirenomelia in Bmp7 and Tsg compound mutant mice: requirement for Bmp signaling in the development of ventral posterior mesoderm. Development 132, 2489–2499.
Zakin, L., Metzinger, C.A., Chang, E.Y., Coffinier, C., De Robertis, E.M., 2008. Development of the vertebral morphogenetic field in the mouse: interactions between Crossveinless-2 and twisted gastrulation. Dev. Biol. 323, 6–18.
Zhang, J.L., Huang, Y., Qiu, L.Y., Nickel, J., Sebald, W., 2007. von Willebrand factor type C domain-containing proteins regulate bone morphogenetic protein signaling through different recognition mechanisms. J. Biol. Chem. 282, 20002–20014.
Zhang, J.L., Qiu, L.Y., Kotzsch, A., Weidauer, S., Patterson, L., Hammerschmidt, M., Sebald, W., Mueller, T.D., 2008. Crystal structure analysis reveals how the Chordin family member crossveinless 2 blocks BMP-2 receptor binding. Dev. Cell 14, 739–750.

LETTERS

Frequent inactivation of A20 in B-cell lymphomas

Motohiro Kato[1,2], Masashi Sanada[1,5], Itaru Kato[6], Yasuharu Sato[7], Junko Takita[1,2,3], Kengo Takeuchi[8], Akira Niwa[6], Yuyan Chen[1,2], Kumi Nakazaki[1,4,5], Junko Nomoto[9], Yoshitaka Asakura[9], Satsuki Muto[1], Azusa Tamura[1], Mitsuru Iio[1], Yoshiki Akatsuka[11], Yasuhide Hayashi[12], Hiraku Mori[13], Takashi Igarashi[2], Mineo Kurokawa[4], Shigeru Chiba[3], Shigeo Mori[14], Yuichi Ishikawa[8], Koji Okamoto[10], Kensei Tobinai[9], Hitoshi Nakagama[10], Tatsutoshi Nakahata[6], Tadashi Yoshino[7], Yukio Kobayashi[9] & Seishi Ogawa[1,5]

A20 is a negative regulator of the NF-κB pathway and was initially identified as being rapidly induced after tumour-necrosis factor-α stimulation[1]. It has a pivotal role in regulation of the immune response and prevents excessive activation of NF-κB in response to a variety of external stimuli[2–7]; recent genetic studies have disclosed putative associations of polymorphic *A20* (also called *TNFAIP3*) alleles with autoimmune disease risk[8,9]. However, the involvement of A20 in the development of human cancers is unknown. Here we show, using a genome-wide analysis of genetic lesions in 238 B-cell lymphomas, that *A20* is a common genetic target in B-lineage lymphomas. A20 is frequently inactivated by somatic mutations and/or deletions in mucosa-associated tissue lymphoma (18 out of 87; 21.8%) and Hodgkin's lymphoma of nodular sclerosis histology (5 out of 15; 33.3%), and, to a lesser extent, in other B-lineage lymphomas. When re-expressed in a lymphoma-derived cell line with no functional *A20* alleles, wild-type A20, but not mutant A20, resulted in suppression of cell growth and induction of apoptosis, accompanied by downregulation of NF-κB activation. The A20-deficient cells stably generated tumours in immunodeficient mice, whereas the tumorigenicity was effectively suppressed by re-expression of A20. In A20-deficient cells, suppression of both cell growth and NF-κB activity due to re-expression of A20 depended, at least partly, on cell-surface-receptor signalling, including the tumour-necrosis factor receptor. Considering the physiological function of A20 in the negative modulation of NF-κB activation induced by multiple upstream stimuli, our findings indicate that uncontrolled signalling of NF-κB caused by loss of A20 function is involved in the pathogenesis of subsets of B-lineage lymphomas.

Malignant lymphomas of B-cell lineages are mature lymphoid neoplasms that arise from various lymphoid tissues[10,11]. To obtain a comprehensive registry of genetic lesions in B-lineage lymphomas, we performed a single nucleotide polymorphism (SNP) array analysis of 238 primary B-cell lymphoma specimens of different histologies, including 64 samples of diffuse large B-cell lymphomas (DLBCLs), 52 follicular lymphomas, 35 mantle cell lymphomas (MCLs), and 87 mucosa-associated tissue (MALT) lymphomas (Supplementary Table 1). Three Hodgkin's-lymphoma-derived cell lines were also analysed. Interrogating more than 250,000 SNP sites, this platform permitted the identification of copy number changes at an average resolution of less than 12 kilobases (kb). The use of large numbers of SNP-specific probes is a unique feature of this platform, and combined with the CNAG/AsCNAR software, enabled accurate determination of 'allele-specific' copy numbers, and thus allowed for sensitive detection of loss of heterozygosity (LOH) even without apparent copy-number reduction, in the presence of up to 70–80% normal cell contamination[12,13].

Lymphoma genomes underwent a wide range of genetic changes, including numerical chromosomal abnormalities and segmental gains and losses of chromosomal material (Supplementary Fig. 1), as well as copy-number-neutral LOH, or uniparental disomy (Supplementary Fig. 2). Each histology type had a unique genomic signature, indicating a distinctive underlying molecular pathogenesis for different histology types (Fig. 1a and Supplementary Fig. 3). On the basis of the genomic signatures, the initial pathological diagnosis of MCL was re-evaluated and corrected to DLBCL in two cases. Although most copy number changes involved large chromosomal segments, a number of regions showed focal gains and deletions, accelerating identification of their candidate gene targets. After excluding known copy number variations, we identified 46 loci showing focal gains (19 loci) or deletions (27 loci) (Supplementary Tables 2 and 3 and Supplementary Fig. 4).

Genetic lesions on the NF-κB pathway were common in B-cell lymphomas and found in approximately 40% of the cases (Supplementary Table 1), underpinning the importance of aberrant NF-κB activation in lymphomagenesis[11,14] in a genome-wide fashion. They included focal gain/amplification at the *REL* locus (16.4%) (Fig. 1b) and *TRAF6* locus (5.9%), as well as focal deletions at the *PTEN* locus (5.5%) (Supplementary Figs 1 and 4). However, the most striking finding was the common deletion at 6q23.3 involving a 143-kb segment. It exclusively contained the *A20* gene (also called *TNFAIP3*), a negative regulator of NF-κB activation[3–7,15] (Fig. 1b), which was previously reported as a candidate target of 6q23 deletions in ocular lymphoma[16]. LOH involving the *A20* locus was found in 50 cases, of which 12 showed homozygous deletions as determined by the loss of both alleles in an allele-specific copy number analysis (Fig. 1b, Table 1 and Supplementary Table 4). On the basis of this finding, we searched for possible tumour-specific mutations of *A20* by genomic DNA sequencing of entire coding exons of the gene in the same series of lymphoma samples (Supplementary Fig. 5). Because two out of the three Hodgkin's-lymphoma-derived cell lines had biallelic *A20* deletions/mutations (Supplementary Fig. 6), 24 primary samples from Hodgkin's lymphoma were also analysed for mutations, where

[1]Cancer Genomics Project, Department of [2]Pediatrics, [3]Cell Therapy and Transplantation Medicine, and [4]Hematology and Oncology, Graduate School of Medicine, University of Tokyo, 7-3-1 Hongo, Bunkyo-ku, Tokyo 113-8655, Japan. [5]Core Research for Evolutional Science and Technology, Japan Science and Technology Agency, 4-1-8, Honcho, Kawaguchi-shi, Saitama 332-0012, Japan. [6]Department of Pediatrics, Graduate School of Medicine, Kyoto University, 54 Kawahara-cho, Shogoin, Sakyo-ku, Kyoto 606-8507, Japan. [7]Department of Pathology, Okayama University Graduate School of Medicine, Dentistry and Pharmaceutical Sciences, 2-5-1 Shikata-cho, Kita-ku, Okayama 700-8558, Japan. [8]Division of Pathology, The Cancer Institute of Japanese Foundation for Cancer Research, Japan, 3-10-6 Ariake, Koto-ku, Tokyo 135-8550, Japan. [9]Hematology Division, Hospital, and [10]Early Oncogenesis Research Project, Research Institute, National Cancer Center, 5-1-1 Tsukiji, Chuo-ku, Tokyo 104-0045, Japan. [11]Division of Immunology, Aichi Cancer Center Research Institute, 1-1 Kanokoden, Chikusa-ku, Nagoya 464-8681, Japan. [12]Gunma Children's Medical Center, 779 Shimohakoda, Hokkitsu-machi, Shibukawa 377-8577, Japan. [13]Division of Hematology, Internal Medicine, Showa University Fujigaoka Hospital, 1-30, Fujigaoka, Aoba-ku, Yokohama-shi, Kanagawa 227-8501, Japan. [14]Department of Pathology, Teikyo University School of Medicine, 2-11-1 Kaga, Itabashi-ku, Tokyo 173-8605, Japan.

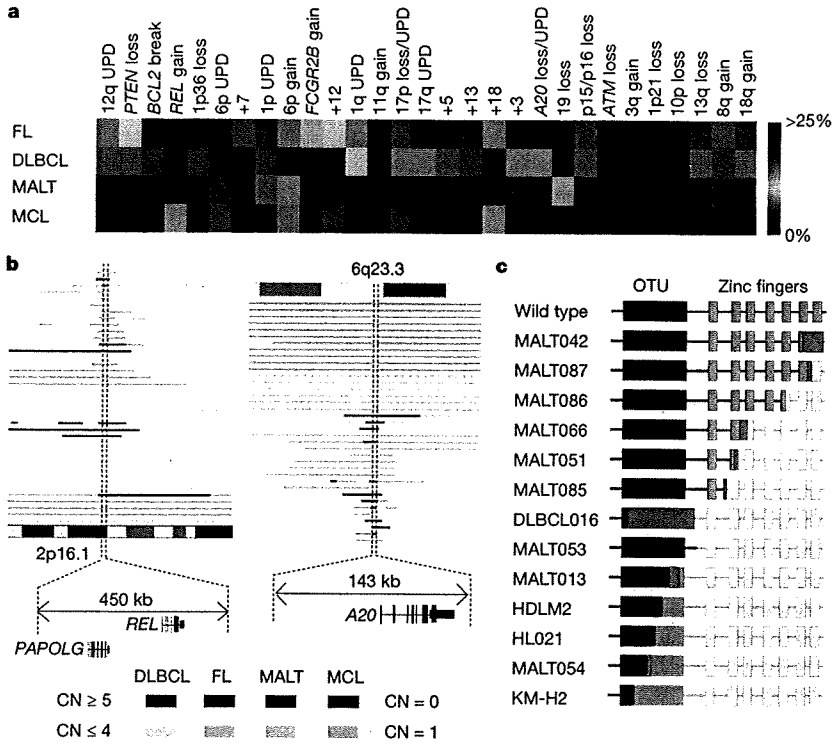

Figure 1 | Genomic signatures of different B-cell lymphomas and common genetic lesions at 2p16-15 and 6q23.3 involving NF-κB pathway genes. **a**, Twenty-nine genetic lesions were found in more than 10% in at least one histology and used for clustering four distinct histology types of B-lineage lymphomas. The frequency of each genetic lesion in each histology type is colour-coded. FL, follicular lymphoma; UPD, uniparental disomy. **b**, Recurrent genetic changes are depicted based on CNAG output of the SNP array analysis of 238 B-lineage lymphoma samples, which include gains at the *REL* locus on 2p16-15 (left panel) and the *A20* locus on 6q23.3 (right panel). Regions showing copy number gain or loss are indicated by horizontal lines. Four histology types are indicated by different colours, where high-grade amplifications and homozygous deletions are shown by darker shades to discriminate from simple gains (copy number ≤4) and losses (copy number = 1) (lighter shades). **c**, Point mutations and small nucleotide insertions and deletions in the *A20* (*TNFAIP3*) gene caused premature truncation of A20 in most cases. Altered amino acids caused by frame shifts are indicated by green bars.

genomic DNA was extracted from 150 microdissected CD30-positive tumour cells (Reed–Sternberg cells) for each sample. *A20* mutations were found in 18 out of 265 lymphoma samples (6.8%) (Table 1), among which 13 mutations, including nonsense mutations (3 cases), frame-shift insertions/deletions (9 cases), and a splicing donor site mutation (1 case) were thought to result in premature termination of translation (Fig. 1c). Four missense mutations and one intronic mutation were identified in five microdissected Hodgkin's lymphoma samples. They were not found in the surrounding normal tissues, and thus, were considered as tumour-specific somatic changes.

In total, biallelic *A20* lesions were found in 31 out of 265 lymphoma samples including 3 Hodgkin's lymphoma cell lines. Quantitative analysis of SNP array data suggested that these *A20* lesions were present in the major tumour fraction within the samples (Supplementary Fig. 7). Inactivation of *A20* was most frequent in MALT lymphoma (18 out of 87) and Hodgkin's lymphoma (7 out of 27), although it was also found in DLBCL (5 out of 64) and follicular lymphoma (1 out of 52) at lower frequencies. In MALT lymphoma, biallelic *A20* lesions were confirmed in 18 out of 24 cases (75.0%) with LOH involving the 6q23.3 segment (Supplementary Fig. 8). Considering the limitation in detecting very small homozygous deletions, *A20* was thought to be the target of 6q23 LOH in MALT lymphoma. On the other hand, the 6q23 LOHs in other histology types tended to be extended into more centromeric regions and less frequently accompanied biallelic *A20* lesions (Supplementary Fig. 8 and Supplementary Table 4), indicating that they might be more heterogeneous with regard to their gene targets. We were unable to analyse Hodgkin's lymphoma samples using SNP arrays owing to insufficient genomic DNA obtained from microdissected samples, and were likely to underestimate the frequency of *A20* inactivation in Hodgkin's lymphoma because we might fail to detect a substantial proportion of cases with homozygous deletions, which explained 50% (12 out of 24) of *A20* inactivation in other histology types. *A20* mutations in Hodgkin's lymphoma were exclusively found in nodular sclerosis classical Hodgkin's lymphoma (5 out of 15) but not in other histology types (0 out of 9), although the possible association requires further confirmation in additional cases.

A20 is a key regulator of NF-κB signalling, negatively modulating NF-κB activation through a wide variety of cell surface receptors and viral proteins, including tumour-necrosis factor (TNF) receptors, toll-like receptors, CD40, as well as Epstein–Barr-virus-associated LMP1 protein[2,5,17,18]. To investigate the role of A20 inactivation in lymphomagenesis, we re-expressed wild-type A20 under a *Tet*-inducible promoter in a lymphoma-derived cell line (KM-H2) that had no functional *A20* alleles (Supplementary Fig. 6), and examined the effect of A20 re-expression on cell proliferation, survival and downstream NF-κB signalling pathways. As shown in Fig. 2a–c and Supplementary Fig. 9, re-expression of wild-type A20 resulted in the suppression of cell proliferation and enhanced apoptosis, and in the concomitant accumulation of IκBβ and IκBε, and downregulation of NF-κB activity. In contrast, re-expression of two lymphoma-derived A20 mutants, $A20^{532Stop}$ or $A20^{750Stop}$, failed to show growth suppression, induction of apoptosis, accumulation of IκBβ and IκBε or downregulation of

Table 1 | Inactivation of A20 in B-lineage lymphomas

Histology	Tissue	Sample	Allele	Uniparental disomy	Exon	Mutation	Biallelic inactivation
DLBCL							5 out of 64 (7.8%)
	Lymph node	DLBCL008	−/−	No	–	–	
	Lymph node	DLBCL016	+/−	No	Ex2	329insA	
	Lymph node	DLBCL022	−/−	No	–	–	
	Lymph node	DLBCL028	−/−	Yes	–	–	
	Lymph node	MCL008*	−/−	Yes	–	–	
Follicular lymphoma							1 out of 52 (1.9%)
	Lymph node	FL024	−/−	No	–	–	
MCL							0 out of 35 (0%)
MALT							18 out of 87 (21.8%)
Stomach							3 out of 23 (13.0%)
	Gastric mucosa	MALT013	+/+	Yes	Ex5	705insG	
	Gastric mucosa	MALT014	+/+	Yes	Ex3	Ex3 donor site>A	
	Gastric mucosa	MALT036	+/−	No	Ex7	delintron6–Ex7†	
Eye							13 out of 43 (30.2%)
	Ocular adnexa	MALT008	−/−	No	–	–	
	Ocular adnexa	MALT017	−/−	No	–	–	
	Ocular adnexa	MALT051	+/−	No	Ex7	1943delTG	
	Ocular adnexa	MALT053	+/+	Yes	Ex6	1016G>A(stop)	
	Ocular adnexa	MALT054	+/−	No	Ex3	502delTC	
	Ocular adnexa	MALT055	−/−	No	–	–	
	Ocular adnexa	MALT066	+/−	No	Ex7	1581insA	
	Ocular adnexa	MALT067	−/−	No	–	–	
	Ocular adnexa	MALT082	−/−	Yes	–	–	
	Ocular adnexa	MALT084	−/−	Yes	–	–	
	Ocular adnexa	MALT085	+/+	Yes	Ex7	1435insG	
	Ocular adnexa	MALT086	+/+	Yes	Ex6	878C>T(stop)	
	Ocular adnexa	MALT087	+/+	Yes	Ex9	2304delGG	
Lung							2 out of 12 (16.7%)
	Lung	MALT042	−/−	No	–	–	
	Lung	MALT047	+/+	Yes	Ex9	2281insT	
Other‡							0 out of 9 (0%)
Hodgkin's lymphoma							7 out of 27 (26.0%)
NSHL	Lymph node	HL10	ND	ND	Ex7	1777G>A(V571I)	
NSHL	Lymph node	HL12	ND	ND	Ex7	1156A>G(R364G)	
NSHL	Lymph node	HL21	ND	ND	Ex4	569G>A(stop)	
NSHL	Lymph node	HL24	ND	ND	Ex3	1487C>A(T474N)	
NSHL	Lymph node	HL23	ND	ND	–	Intron 3§	
	Cell line	KM-H2	−/−	No	–		
	Cell line	HDLM2	+/−	No	Ex4	616ins29bp‖	
Total							31 out of 265 (11.7%)

DLBCL, diffuse large B-cell lymphoma; MALT, MALT lymphoma; MCL, mantle cell lymphoma; ND, not determined because SNP array analysis was not performed; NSHL, nodular sclerosis classical Hodgkin's lymphoma.
* Diagnosis was changed based on the genomic data, which was confirmed by re-examination of pathology.
† Deletion including the boundary of intron 6 and exon 7 (see also Supplementary Fig. 5b).
‡ Including 1 parotid gland, 1 salivary gland, 2 colon and 5 thyroid cases.
§ Insertion of CTC at −19 bases from the beginning of exon 3.
‖ Insertion of TGGCTTCCACAGACACACCCATGGCCCGA.

NF-κB activity (Fig. 2a–c), indicating that these were actually loss-of-function mutations. To investigate the role of A20 inactivation in lymphomagenesis *in vivo*, *A20*- and mock-transduced KM-H2 cells were transplanted in NOD/SCID/γ_c^{null} (NOG) mice[19], and their tumour formation status was examined for 5 weeks with or without induction of wild-type A20 by tetracycline administration. As shown in Fig. 2d, mock-transduced cells developed tumours at the injected sites, whereas the *Tet*-inducible *A20*-transduced cells generated tumours only in the absence of A20 induction (Supplementary Table 5), further supporting the tumour suppressor role of A20 in lymphoma development.

Given the mode of negative regulation of NF-κB signalling, we next investigated the origins of NF-κB activity that was deregulated by A20 loss in KM-H2 cells. The conditioned medium prepared from a 48-h serum-free KM-H2 culture had increased NF-κB upregulatory activity compared with fresh serum-free medium, which was inhibited by re-expression of A20 (Fig. 3a). KM-H2 cells secreted two known ligands for TNF receptor—TNF-α and lymphotoxin-α (Supplementary Fig. 10)[20]—and adding neutralizing antibodies against these cytokines into cultures significantly suppressed their cell growth and NF-κB activity without affecting the levels of their overall suppression after A20 induction (Fig. 3b, d). In addition, recombinant TNF-α and/or lymphotoxin-α added to fresh serum-free medium promoted cell growth and NF-κB activation in KM-H2 culture, which were again suppressed by re-expression of A20 (Fig. 3c, e). Although our data in Fig. 3 also show the presence of factors other than TNF-α and lymphotoxin-α in the KM-H2-conditioned medium—as well as some intrinsic pathways in the cell (Fig. 3a)—that were responsible for the A20-dependent NF-κB activation, these results indicate that both cell growth and NF-κB activity that were upregulated by A20 inactivation depend at least partly on the upstream stimuli that evoked the NF-κB-activating signals.

Aberrant activation of the NF-κB pathway is a hallmark of several subtypes of B-lineage lymphomas, including Hodgkin's lymphoma, MALT lymphoma, and a subset of DLBCL, as well as other lymphoid neoplasms[11,14], where a number of genetic alterations of NF-κB signalling pathway genes[21–25], as well as some viral proteins[26,27], have been implicated in the aberrant activation of the NF-κB pathway[14]. Thus, frequent inactivation of A20 in Hodgkin's lymphoma and MALT and other lymphomas provides a novel insight into the molecular pathogenesis of these subtypes of B-lineage lymphomas through deregulated NF-κB activation. Because A20 provides a

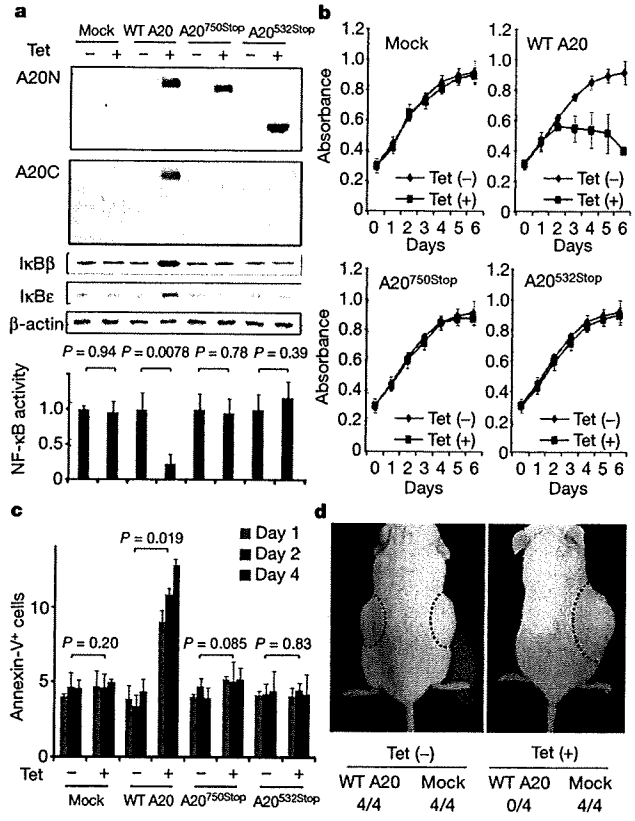

Figure 2 | Effects of wild-type and mutant A20 re-expressed in a lymphoma cell line that lacks the normal *A20* gene. **a**, Western blot analyses of wild-type (WT) and mutant ($A20^{532Stop}$ and $A20^{750Stop}$) A20, as well as IκBβ and IκBε, in KM-H2 cells, in the presence or absence of tetracycline treatment (top panels). A20N and A20C are polyclonal antisera raised against N-terminal and C-terminal A20 peptides, respectively. β-actin blots are provided as a control. NF-κB activities are expressed as mean absorbance ± s.d. ($n = 6$) in luciferase assays (bottom panel). **b**, Proliferation of KM-H2 cells stably transduced with plasmids for mock and *Tet*-inducible wild-type A20, $A20^{532Stop}$ and $A20^{750Stop}$ was measured using a cell counting kit in the presence (red lines) or absence (blue lines) of tetracycline. Mean absorbance ± s.d. ($n = 5$) is plotted. **c**, The fractions of Annexin-V-positive KM-H2 cells transduced with various *Tet*-inducible A20 constructs were measured by flow cytometry after tetracycline treatment and the mean values (±s.d., $n = 3$) are plotted. **d**, *In vivo* tumorigenicity was assayed by inoculating 7×10^6 KM-H2 cells transduced with mock or *Tet*-inducible wild-type A20 in NOG mice, with (right panel) or without (left panel) tetracycline administration.

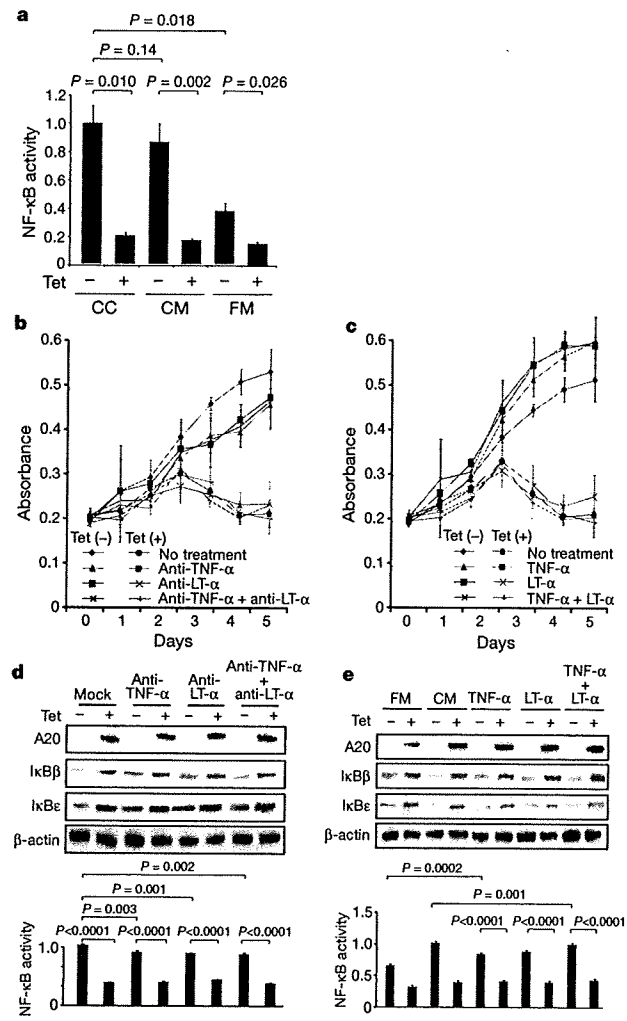

Figure 3 | Tumour suppressor role of A20 under external stimuli. **a**, NF-κB activity in KM-H2 cells was measured 30 min after cells were inoculated into fresh medium (FM) or KM-H2-conditioned medium (CM) obtained from the 48-h culture of KM-H2, and was compared with the activity after 48 h continuous culture of KM-H2 (CC). A20 was induced 12 h before inoculation in Tet (+) groups. **b**, **c**, Effects of neutralizing antibodies against TNF-α and lymphotoxin-α (LTα) (**b**) and of recombinant TNF-α and LT-α added to the culture (**c**) on cell growth were evaluated in the presence (Tet (+)) or absence (Tet (−)) of A20 induction. Cell numbers were measured using a cell counting kit and are plotted as their mean absorbance ± s.d. ($n = 6$). **d**, **e**, Effects of the neutralizing antibodies (**d**) and the recombinant cytokines added to the culture (**e**) on NF-κB activities and the levels of IκBβ and IκBε after 48 h culture with (Tet (+)) or without (Tet (−)) tetracycline treatment. NF-κB activities are expressed as mean absorbance ± s.d. ($n = 6$) in luciferase assays.

negative feedback mechanism in the regulation of NF-κB signalling pathways upon a variety of stimuli, aberrant activation of NF-κB will be a logical consequence of A20 inactivation. However, there is also the possibility that the aberrant NF-κB activity of A20-inactivated lymphoma cells is derived from upstream stimuli, which may be from the cellular environment. In this context, it is intriguing that MALT lymphoma usually arises at the site of chronic inflammation caused by infection or autoimmune disorders and may show spontaneous regression after eradication of infectious organisms[28]; furthermore, Hodgkin's lymphoma frequently shows deregulated cytokine production from Reed–Sternberg cells and/or surrounding reactive cells[29]. Detailed characterization of the NF-κB pathway regulated by A20 in both normal and neoplastic B lymphocytes will promote our understanding of the precise roles of A20 inactivation in the pathogenesis of these lymphoma types. Our finding underscores the importance of genome-wide approaches in the identification of genetic targets in human cancers.

METHODS SUMMARY

Genomic DNA from 238 patients with non-Hodgkin's lymphoma and three Hodgkin's-lymphoma-derived cell lines was analysed using GeneChip SNP genotyping microarrays (Affymetrix). This study was approved by the ethics boards of the University of Tokyo, National Cancer Institute Hospital, Okayama University, and the Cancer Institute of the Japanese Foundation of Cancer Research. After appropriate normalization of mean array intensities, signal ratios between tumours and anonymous normal references were calculated in an allele-specific manner, and allele-specific copy numbers were inferred from the observed signal ratios based on the hidden Markov model using CNAG/AsCNAR software (http://www.genome.umin.jp). *A20* mutations were examined by directly sequencing genomic DNA using a set of primers (Supplementary Table 6). Full-length cDNAs of wild-type and mutant *A20* were introduced into a

lentivirus vector, pLenti4/TO/V5-DEST (Invitrogen), with a *Tet*-inducible promoter. Viral stocks were prepared by transfecting the vector plasmids into 293FT cells (Invitrogen) using the calcium phosphate method and then infected to the KM-H2 cell line. Proliferation of KM-H2 cells was measured using a Cell Counting Kit (Dojindo). Western blot analyses and luciferase assays were performed as previously described. NF-κB activity was measured by luciferase assays in KM-H2 cells stably transduced with a reporter plasmid having an NF-κB response element, pGL4.32 (Promega). Apoptosis of KM-H2 upon A20 induction was evaluated by counting Annexin-V-positive cells by flow cytometry. For *in vivo* tumorigenicity assays, 7×10^6 KM-H2 cells were transduced with the *Tet*-inducible *A20* gene and those with a mock vector were inoculated on the contralateral sides in eight NOG mice[19] and examined for their tumour formation with ($n = 4$) or without ($n = 4$) tetracycline administration. Full copy number data of the 238 lymphoma samples will be accessible from the Gene Expression Omnibus (GEO, http://ncbi.nlm.nih.gov/geo/) with the accession number GSE12906.

Full Methods and any associated references are available in the online version of the paper at www.nature.com/nature.

Received 17 September 2008; accepted 3 March 2009.
Published online 3 May 2009.

1. Dixit, V. M. *et al.* Tumor necrosis factor-α induction of novel gene products in human endothelial cells including a macrophage-specific chemotaxin. *J. Biol. Chem.* **265**, 2973–2978 (1990).
2. Song, H. Y., Rothe, M. & Goeddel, D. V. The tumor necrosis factor-inducible zinc finger protein A20 interacts with TRAF1/TRAF2 and inhibits NF-κB activation. *Proc. Natl Acad. Sci. USA* **93**, 6721–6725 (1996).
3. Lee, E. G. *et al.* Failure to regulate TNF-induced NF-κB and cell death responses in A20-deficient mice. *Science* **289**, 2350–2354 (2000).
4. Boone, D. L. *et al.* The ubiquitin-modifying enzyme A20 is required for termination of Toll-like receptor responses. *Nature Immunol.* **5**, 1052–1060 (2004).
5. Wang, Y. Y., Li, L., Han, K. J., Zhai, Z. & Shu, H. B. A20 is a potent inhibitor of TLR3- and Sendai virus-induced activation of NF-κB and ISRE and IFN-β promoter. *FEBS Lett.* **576**, 86–90 (2004).
6. Wertz, I. E. *et al.* De-ubiquitination and ubiquitin ligase domains of A20 downregulate NF-κB signalling. *Nature* **430**, 694–699 (2004).
7. Heyninck, K. & Beyaert, R. A20 inhibits NF-κB activation by dual ubiquitin-editing functions. *Trends Biochem. Sci.* **30**, 1–4 (2005).
8. Graham, R. R. *et al.* Genetic variants near *TNFAIP3* on 6q23 are associated with systemic lupus erythematosus. *Nature Genet.* **40**, 1059–1061 (2008).
9. Musone, S. L. *et al.* Multiple polymorphisms in the *TNFAIP3* region are independently associated with systemic lupus erythematosus. *Nature Genet.* **40**, 1062–1064 (2008).
10. Jaffe, E. S., Harris, N. L., Stein, H. & Vardiman, J. W. *World Health Organization Classification of Tumours. Pathology and Genetics of Tumours of Hematopoietic and Lymphoid Tissues* (IARC Press, 2001).
11. Klein, U. & Dalla-Favera, R. Germinal centres: role in B-cell physiology and malignancy. *Nature Rev. Immunol.* **8**, 22–33 (2008).
12. Nannya, Y. *et al.* A robust algorithm for copy number detection using high-density oligonucleotide single nucleotide polymorphism genotyping arrays. *Cancer Res.* **65**, 6071–6079 (2005).
13. Yamamoto, G. *et al.* Highly sensitive method for genomewide detection of allelic composition in nonpaired, primary tumor specimens by use of affymetrix single-nucleotide-polymorphism genotyping microarrays. *Am. J. Hum. Genet.* **81**, 114–126 (2007).
14. Jost, P. J. & Ruland, J. Aberrant NF-κB signaling in lymphoma: mechanisms, consequences, and therapeutic implications. *Blood* **109**, 2700–2707 (2007).
15. Durkop, H., Hirsch, B., Hahn, C., Foss, H. D. & Stein, H. Differential expression and function of A20 and TRAF1 in Hodgkin lymphoma and anaplastic large cell lymphoma and their induction by CD30 stimulation. *J. Pathol.* **200**, 229–239 (2003).
16. Honma, K. *et al. TNFAIP3* is the target gene of chromosome band 6q23.3-q24.1 loss in ocular adnexal marginal zone B cell lymphoma. *Genes Chromosom. Cancer* **47**, 1–7 (2008).
17. Sarma, V. *et al.* Activation of the B-cell surface receptor CD40 induces A20, a novel zinc finger protein that inhibits apoptosis. *J. Biol. Chem.* **270**, 12343–12346 (1995).
18. Fries, K. L., Miller, W. E. & Raab-Traub, N. The A20 protein interacts with the Epstein-Barr virus latent membrane protein 1 (LMP1) and alters the LMP1/TRAF1/TRADD complex. *Virology* **264**, 159–166 (1999).
19. Hiramatsu, H. *et al.* Complete reconstitution of human lymphocytes from cord blood $CD34^+$ cells using the NOD/SCID/γ^{null} mice model. *Blood* **102**, 873–880 (2003).
20. Hsu, P. L. & Hsu, S. M. Production of tumor necrosis factor-α and lymphotoxin by cells of Hodgkin's neoplastic cell lines HDLM-1 and KM-H2. *Am. J. Pathol.* **135**, 735–745 (1989).
21. Dierlamm, J. *et al.* The apoptosis inhibitor gene *API2* and a novel 18q gene, *MLT*, are recurrently rearranged in the t(11;18)(q21;q21) associated with mucosa-associated lymphoid tissue lymphomas. *Blood* **93**, 3601–3609 (1999).
22. Willis, T. G. *et al.* Bcl10 is involved in t(1;14)(p22;q32) of MALT B cell lymphoma and mutated in multiple tumor types. *Cell* **96**, 35–45 (1999).
23. Joos, S. *et al.* Classical Hodgkin lymphoma is characterized by recurrent copy number gains of the short arm of chromosome 2. *Blood* **99**, 1381–1387 (2002).
24. Martin-Subero, J. I. *et al.* Recurrent involvement of the *REL* and *BCL11A* loci in classical Hodgkin lymphoma. *Blood* **99**, 1474–1477 (2002).
25. Lenz, G. *et al.* Oncogenic *CARD11* mutations in human diffuse large B cell lymphoma. *Science* **319**, 1676–1679 (2008).
26. Deacon, E. M. *et al.* Epstein-Barr virus and Hodgkin's disease: transcriptional analysis of virus latency in the malignant cells. *J. Exp. Med.* **177**, 339–349 (1993).
27. Yin, M. J. *et al.* HTLV-I Tax protein binds to MEKK1 to stimulate IκB kinase activity and NF-κB activation. *Cell* **93**, 875–884 (1998).
28. Isaacson, P. G. & Du, M. Q. MALT lymphoma: from morphology to molecules. *Nature Rev. Cancer* **4**, 644–653 (2004).
29. Skinnider, B. F. & Mak, T. W. The role of cytokines in classical Hodgkin lymphoma. *Blood* **99**, 4283–4297 (2002).

Supplementary Information is linked to the online version of the paper at www.nature.com/nature.

Acknowledgements This work was supported by the Core Research for Evolutional Science and Technology, Japan Science and Technology Agency, by the 21st century centre of excellence program 'Study on diseases caused by environment/genome interactions', and by Grant-in-Aids from the Ministry of Education, Culture, Sports, Science and Technology of Japan and from the Ministry of Health, Labor and Welfare of Japan for the 3rd-term Comprehensive 10-year Strategy for Cancer Control. We also thank Y. Ogino, E. Matsui and M. Matsumura for their technical assistance.

Author Contributions M.Ka., K.N. and M.S. performed microarray experiments and subsequent data analyses. M.Ka., Y.C., K.Ta., J.T., J.N., M.I., A.T. and Y.K. performed mutation analyses of *A20*. M.Ka., S.Mu., M.S., Y.C. and Y.Ak. conducted functional assays of mutant A20. Y.S., K.Ta., Y.As., H.M., M.Ku., S.Mo., S.C., Y.K., K.To. and Y.I. prepared tumour specimens. I.K., K.O., A.N., H.N. and T.N. conducted *in vivo* tumorigenicity experiments in NOG/SCID mice. T.I., Y.H., T.Y., Y.K. and S.O. designed overall studies, and S.O. wrote the manuscript. All authors discussed the results and commented on the manuscript.

Author Information The copy number data as well as the raw microarray data will be accessible from the GEO (http://ncbi.nlm.nih.gov/geo/) with the accession number GSE12906. Reprints and permissions information is available at www.nature.com/reprints. Correspondence and requests for materials should be addressed to S.O. (sogawa-tky@umin.ac.jp) or Y.K. (ykkobaya@ncc.go.jp).

METHODS

Specimens. Primary tumour specimens were obtained from patients who were diagnosed with DLBCL, follicular lymphoma, MCL, MALT lymphoma, or classical Hodgkin's lymphoma. In total, 238 primary lymphoma specimens listed in Supplementary Table 1 were subjected to SNP array analysis. Three Hodgkin's-lymphoma-derived cell lines (KM-H2, HDLM2, L540) were obtained from Hayashibara Biochemical Laboratories, Inc., Fujisaki Cell Center and were also analysed by SNP array analysis.

Microarray analysis. High-molecular-mass DNA was isolated from tumour specimens and subjected to SNP array analysis using GeneChip Mapping 50K and/or 250K arrays (Affymetrix). The scanned array images were processed with Gene Chip Operation software (GCOS), followed by SNP calls using GTYPE. Genome-wide copy number measurements and LOH detection were performed using CNAG/AsCNAR software[12,13].

Mutation analysis. Mutations in the *A20* gene were examined in 265 samples of B-lineage lymphoma, including 62 DLBCLs, 52 follicular lymphomas, 87 MALTs, 37 MCLs and 3 Hodgkin's-lymphoma-derived cell lines and 24 primary Hodgkin's lymphoma samples, by direct sequencing using an ABI PRISM 3130xl Genetic Analyser (Applied Biosystems). To analyse primary Hodgkin's lymphoma samples in which CD30-positive tumour cells (Reed–Sternberg cells) account for only a fraction of the specimen, 150 Reed–Sternberg cells were collected for each 10 μm slice of a formalin-fixed block immunostained for CD30 by laser-capture microdissection (ASLMD6000, Leica), followed by genomic DNA extraction using QIAamp DNA Micro kit (Qiagen). The primer sets used in this study are listed in Supplementary Table 6.

Functional analysis of wild-type and mutant A20. Full-length cDNA for wild-type *A20* was isolated from total RNA extracted from an acute myeloid leukaemia-derived cell line, CTS, and subcloned into a lentivirus vector (pLenti4/TO/V5-DEST, Invitrogen). cDNAs for mutant A20 were generated by PCR amplification using mutagenic primers (Supplementary Table 6), and introduced into the same lentivirus vector. Forty-eight hours after transfection of each plasmid into 293FT cells using the calcium phosphate method, lentivirus stocks were obtained from ultrafiltration using Amicon Ultra (Millipore), and used to infect KM-H2 cells to generate stable transfectants of mock, wild-type and mutant A20. Each KM-H2 derivative cell line was further transduced stably with a reporter plasmid (pGL4.32, Promega) containing a luciferase gene under an NF-κB-responsive element by electroporation using Nucleofector reagents (Amaxa).

Assays for cell proliferation and NF-κB activity. Proliferation of the KM-H2 derivative cell lines was assayed in triplicate using a Cell Counting Kit (Dojindo). The mean absorption of five independent assays was plotted with s.d. for each derivative line. Two independent KM-H2-derived cell lines were used for each experiment. The NF-κB activity in KM-H2 derivatives for A20 mutants was evaluated by luciferase assays using a PiccaGene Luciferase Assay Kit (TOYO B-Net Co.). Each assay was performed in triplicate and the mean absorption of five independent experiments was plotted with s.d.

Western blot analyses. Polyclonal anti-sera against N-terminal (anti-A20N) and C-terminal (anti-A20C) A20 peptides were generated by immunizing rabbits with these peptides (LSNMRKAVKIRERTPEDIC for anti-A20N and CFQFKQMYG for anti-A20C, respectively). Total cell lysates from KM-H2 cells were separated on 7.5% polyacrylamide gel and subjected to western blot analysis using antibodies to A20 (anti-A20N and anti-A20C), IκBα (sc-847), IκBβ (sc-945), IκBγ (sc-7155) and actin (sc-8432) (Santa Cruz Biotechnology).

Functional analyses of wild-type and mutant A20. Each KM-H2 derivative cell line stably transduced with various *Tet*-inducible A20 constructs was cultured in serum-free medium in the presence or absence of A20 induction using 1 μg ml^{-1} of tetracycline, and cell number was counted every day. 1×10^6 cells of each KM-H2 derivative cell line were analysed for their intracellular levels of IκBβ and IκBε and for NF-κB activities by western blot analyses and luciferase assays, respectively, 12 h after the beginning of cell culture. Effects of human recombinant TNF-α and lymphotoxin-α (210-TA and 211-TB, respectively, R&D Systems) on the NF-κB pathway and cell proliferation were evaluated by adding both cytokines into 10 ml of serum-free cell culture at a concentration of 200 pg ml^{-1}. For cell proliferation assays, culture medium was half replaced every 12 h to minimize the side-effects of autocrine cytokines. Intracellular levels of IκBβ, IκBε and NF-κB were examined 12 h after the beginning of the cell culture. To evaluate the effect of neutralizing TNF-α and lymphotoxin-α, 1×10^6 of KM-H2 cells transduced with both *Tet*-inducible A20 and the NF-κB-luciferase reporter were pre-cultured in serum-free media for 36 h, and thereafter neutralizing antibodies against TNF-α (MAB210, R&D Systems) and/or lymphotoxin-α (AF-211-NA, R&D Systems) were added to the media at a concentration of 200 pg ml^{-1}. After the extended culture during 12 h with or without 1 μg ml^{-1} tetracycline, the intracellular levels of IκBβ and IκBε and NF-κB activities were examined by western blot analysis and luciferase assays, respectively. To examine the effects of A20 re-expression on apoptosis, 1×10^6 KM-H2 cells were cultured for 4 days in 10 ml medium with or without *Tet* induction. After staining with phycoerythrin-conjugated anti-Annexin-V (ID556422, Becton Dickinson), Annexin-V-positive cells were counted by flow cytometry at the indicated times.

***In vivo* tumorigenicity assays.** KM-H2 cells transduced with a mock or *Tet*-inducible wild-type *A20* gene were inoculated into NOG mice and their tumorigenicity was examined for 5 weeks with or without tetracycline administration. Injections of 7×10^6 cells of each KM-H2 cell line were administered to two opposite sites in four mice. Tetracycline was administered in drinking water at a concentration of 200 μg ml^{-1}.

ELISA. Concentrations of TNF-α, lymphotoxin-α, IL-1, IL-2, IL-4, IL-6, IL-12, IL-18 and TGF-β in the culture medium were measured after 48 h using ELISA. For those cytokines detectable after 48-h culture (TNFα, LTα, and IL-6), their time course was examined further using the Quantikine ELISA kit (R&D Systems).

Statistical analysis. Significance of the difference in NF-κB activity between two given groups was evaluated using a paired *t*-test, in which the data from each independent luciferase assay were paired to calculate test statistics. To evaluate the effect of A20 re-expression in KM-H2 cells on apoptosis, the difference in the fractions of Annexin-V-positive cells between Tet (+) and Tet (−) groups was also tested by a paired *t*-test for assays, in which the data from the assays performed on the same day were paired.

Systemic Delivery of Synthetic MicroRNA-16 Inhibits the Growth of Metastatic Prostate Tumors via Downregulation of Multiple Cell-cycle Genes

Fumitaka Takeshita[1], Lubna Patrawala[2,3], Mitsuhiko Osaki[1,4], Ryou-u Takahashi[1], Yusuke Yamamoto[1,5], Nobuyoshi Kosaka[1], Masaki Kawamata[1], Kevin Kelnar[2,3], Andreas G. Bader[2,3], David Brown[2,3] and Takahiro Ochiya[1]

[1]Section for Studies on Metastasis, National Cancer Center Research Institute, Tokyo, Japan; [2]Asuragen, Inc., Austin, Texas, USA; [3]Mima Therapeutics, Inc., Austin, Texas, USA; [4]Division of Molecular Genetics and Biofunction, Tottori University Graduate School of Medical Science, Tottori, Japan; [5]Department of Biology, School of Education, Waseda University, Tokyo, Japan

Recent reports have linked the expression of specific microRNAs (miRNAs) with tumorigenesis and metastasis. Here, we show that microRNA (miR)-16, which is expressed at lower levels in prostate cancer cells, affects the proliferation of human prostate cancer cell lines both *in vitro* and *in vivo*. Transient transfection with synthetic miR-16 significantly reduced cell proliferation of 22Rv1, Du145, PPC-1, and PC-3M-luc cells. A prostate cancer xenograft model revealed that atelocollagen could efficiently deliver synthetic miR-16 to tumor cells on bone tissues in mice when injected into tail veins. In the therapeutic bone metastasis model, injection of miR-16 with atelocollagen via tail vein significantly inhibited the growth of prostate tumors in bone. Cell model studies indicate that miR-16 likely suppresses prostate tumor growth by regulating the expression of genes such as *CDK1* and *CDK2* associated with cell-cycle control and cellular proliferation. There is a trend toward lower miR-16 expression in human prostate tumors versus normal prostate tissues. Thus, this study indicates the therapeutic potential of miRNA in an animal model of cancer metastasis with systemic miRNA injection and suggest that systemic delivery of miR-16 could be used to treat patients with advanced prostate cancer.

Received 21 May 2009; accepted 12 August 2009; published online 8 September 2009. doi:10.1038/mt.2009.207

INTRODUCTION

Advanced prostate cancer is frequently difficult to treat and causes substantial symptoms, including severe pain from metastasis to bone or other sites. Numerous experimental therapeutics are being pursued in clinical trials and offer some hope of improved treatments, but most have so far demonstrated only modest results.

Mounting evidence suggests that the altered expression of specific microRNA's (miRNA's) accuracy contributes to the development of a variety of cancers. Cancer types including prostate cancers can be classified based on their distinct miRNA expression profiles.[1–5]

MiRNAs have been implicated in prostate cancer. Volinia *et al.* identified >40 miRNAs with expression levels that were significantly different in prostate tumors versus normal prostate tissue.[5] Furthermore, the need for additional therapies in metastasis due to hormone-refractory prostate cancer is considerable. Mattie *et al.* found that miRNA expression in human prostate cancer cell lines could distinguish androgen hormone–insensitive PC3 from hormone-sensitive LNCaP cells.[6] LNCaP cells showed upregulation of microRNA (miR)-200c, miR-195, and several let-7 family members, whereas miR-10a, miR-27b, miR-221, miR-222, and mir-210 were lower than in PC3. The serum prostate-specific antigen is the most useful tumor marker for diagnosis and monitoring of prostate cancer. However, its low specificity in distinguishing prostate carcinoma from benign prostatic hyperplasia limits its use as an early detection biomarker. Investigators used custom designed arrays to compare the expression profiles of 319 miRNAs in prostate tumors, cancer cell lines, xenografts, and benign prostatic hyperplasia.[7] MiRNAs could be used to cluster the androgen receptor status of cell lines and xenografts. Among a small set of benign prostatic hyperplasia, hormone refractory, and untreated prostate carcinomas they found 51 differentially expressed miRNAs, 37 of which were downregulated. MiRNAs in this set accurately clustered the benign prostatic hyperplasia, untreated and hormone-refractory prostate carcinomas providing evidence that miRNA expression profiles are altered by changes in disease status. More recently, Bonci *et al.* showed that miR-15a and miR-16-1 cluster inhibit the tumor cell proliferation and invasion via targets CCND1 (cyclinD1), WNT3A, and BCL2 in prostate cancer cell line and clinical samples.[8] These miR-15a and miR-16-1 were coded on chromosome 9 13q14. In this region, loss of heterogeneity was detected in chronic lymphocytic leukemia[9] and prostate cancer patients.[10] These results suggest that miR-15a and/or miR-16 could be a novel target for prostate cancer therapy.

To supplement the expression studies that have been published for prostate cancer, we used a library of synthetic miRNAs

Correspondence: Takahiro Ochiya, Section for Studies on Metastasis, National Cancer Center Research Institute, 1-1, Tsukiji 5-chome, Chuo-ku, Tokyo 104-0045, Japan. E-mail: tochiya@ncc.go.jp

to identify the small RNAs that alter the proliferation of prostate cancer cells. Among the miRNAs that were identified in a functional screen featuring 22Rv1 prostate cancer cells was miR-16, an miRNA that has been implicated in chronic lymphocytic leukemia[1,11,12] and prostate cancer.[8,10] Our studies of miR-16 revealed that it has the capacity to affect the proliferation of a variety of human-derived prostate cancer cells. For the evaluation of miRNA therapy for bone metastasis of prostate cancer, the mouse model of bone-metastatic prostate cancer using bioluminescence-based *in vivo* imaging analysis was selected. We have already established small-interfering RNA (siRNA) molecules that can be delivered to tumor cells in a bone metastatic site using an atelocollagen delivery method.[13] The properties of synthetic miRNA molecules are similar to synthetic siRNA; therefore, it is speculated that synthetic miRNA can also be used for systemic treatment mediated by atelocollagen. In this article, the systemic delivery of synthetic miR-16 using atelocollagen inhibited bone-metastatic human prostate tumor growth in a mouse bone site. We further analyzed the altered expression of cancer-related genes in miR-16-transfected prostate cancer cells and verified that genes associated with cell-cycle progression were mostly affected by miR-16. These results suggest a therapeutic potency of miR-16 in bone-metastatic prostate cancer.

RESULTS

Effect of miR-16 on proliferation of human prostate cancer cell lines

22Rv1 prostate cancer cells were transiently transfected in triplicate with individual synthetic mimics for ~200 miRNAs. Three days after transfection, the cells were monitored for proliferation and apoptotic activity. Among the most active miRNAs identified in the functional screen was miR-16, which reduced the proliferation of the prostate cancer cells by 25% and increased apoptosis by 40% (data not shown). Follow-up studies for measuring the proliferation; using the alamar blue assay with another prostate cancer cell line, PC-3M-luc, revealed that miR-16 reduces proliferation by 60% (**Figure 1a**) relative to the cells transfected with a negative control (NC) miRNA. Further studies of the antiproliferative effect of miR-16 on prostate cancer cells revealed that synthetic miRNA can significantly affect the expansion of cultured 22Rv1, PPC-1, and Du145 cells (**Figure 1a**). The only prostate cancer cell line that proved to be unaffected by the transfection of miR-16 was LNCaP (**Figure 1a**). The amount of miR-16 in the PC-3M-luc cells transfected with synthetic miR-16 was >500-fold higher than that in the control cells (**Figure 1b**). This result suggests that the induced increase of intracellular miR-16 concentrations is capable of suppressing the proliferation of the prostate cancer cells.

miR-16 expression levels in prostate cancer cell lines

Although four of the five prostate cancer cell lines exhibit significant reductions in proliferation following transfection with synthetic miR-16, it is interesting that there is a variation in the level of the effect. To address whether this might be due to variation in the levels of endogenous miR-16 in the various cell lines, we used quantitative reverse transcription (qRT)-PCR to measure the relative abundance of mature miRNA. As shown in **Figure 1c**, most of the cell lines expressed miR-16 at reduced levels. The extent

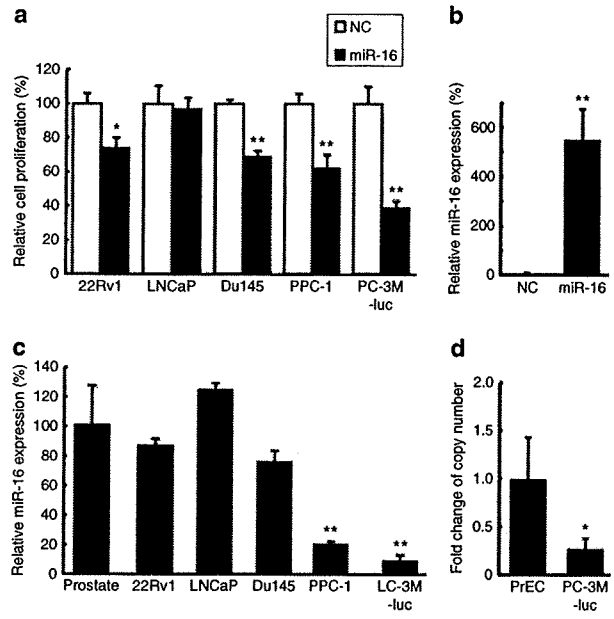

Figure 1 The expression and function of miR-16 in human prostate cancer cell lines. (**a**) Effect of miR-16 on proliferation of human prostate cancer cell lines. Percent (%) proliferation values were normalized to values from cells treated with negative control (NC) microRNA (miRNA). Data represent the mean ($n = 4$) ± SD $^*P < 0.05$, $^{**}P < 0.01$ versus NC miRNA. (**b**) The amount of miR-16 in PC-3M-luc cells transfected with synthetic miR-16. The cellular level of miR-16 was detected by quantitative PCR. The data represent the mean ($n = 3$) ± SD $^{**}P < 0.01$ versus NC miRNA. (**c**) Expression level of miR-16 in human prostate cancer cell lines. The relative expression of miR-16 for each of the cell lines was calculated by comparing the level in normal prostate tissue samples. The data represent the mean ($n = 3$) ± SD $^{**}P < 0.01$ versus normal human prostate tissue. (**d**) The copy number change of the miR-16 loci on chromosome 13q14 in PC-3M-luc cells. The copy number of miR-16 genes were quantified by real-time PCR with genomic DNA. Cultured normal human prostate epithelial cells (PrEC) was used as the control for this experiment for comparison to the PC-3M-luc cells. The data represent the mean ($n = 3$) ± SD $^*P < 0.05$ versus PrEC.

of downregulation correlated with the phenotypic response in these cell lines: *e.g.*, PPC-1 and PC-3M-luc cells, which showed the strongest response to miR-16, had the lowest levels of endogenous miR-16 (**Figure 1a**). The DNA copy numbers on chromosome 13q14, a genomic region that is frequently deleted in chronic lymphocytic leukemia and prostate cancer[14] in the PC-3M-luc cells were reduced to half that of normal prostate cells (**Figure 1d**). However, because the DNA sequence data did not show any mutations on chromosomes coding miR-16 of other copy in the PC-3M-luc cells (data not shown), the remarkable reduction of miR-16 expression might be invoked by a combination of DNA copy number alteration and other factors to affect the expression. LNCaP cells, which showed no response to the miR-16 mimic, were the only cells that tend to have higher miR-16 expression levels than the normal prostate (**Figure 1c**). Additionally, the transfection of miRNAs, which are not downregulated in PC-3M-luc cells, such as miR-10a and miR-188, did not inhibit the growth of PC-3M-luc cells (data not shown). The expression and function data suggest that reduced expression of miR-16 is critical for sustained proliferation in some prostate

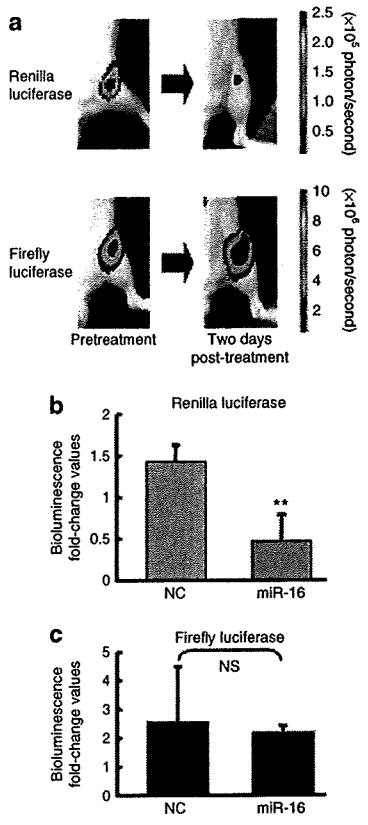

Figure 2 Evaluation of delivery for synthetic microRNA (miRNA) molecules to tumors in bone. A dual-luciferase expressing PC-3M cells that have 3′-UTR of Bcl2 under the renilla luciferase gene, PC-3M-luc/Rluc-Bcl2 3′UTR cells, were generated. These cells were used for dual assay system, for monitoring of tumor growth by firefly luciferase, for monitoring of delivery efficacy of synthetic miR-16 by renilla luciferase. (**a**) Representative images of bone metastasis in the femur of mice. To examine the efficacy of synthetic miR-16 in tumor cells, PC-3M-luc/Rluc-Bcl2 3′UTR cells were injected into the heart of nude mice. Nine weeks after tumor injection, bioluminescence from renilla luciferase was detected. Intravenous injection of miR-16 complexed with atelocollagen suppressed the expression of renilla luciferase (top). In contrast, bioluminescence from firefly luciferase was not affected (bottom). (**b**) Normalized fold change (2 days post/pre-miR-16 administration) of bioluminescence emitted from whole body of mice. This figure is graphically shown of the results of **Figure 2a** by fold change of photon counts. Data represent the mean (n = 3) ± SD *P < 0.01 versus NC miRNA. NS, not significant. NC, negative control.

cancer cell lines and that reintroduction of miR-16 can interfere with that phenotype.

Evaluation of miRNA delivery to bone-metastatic tumors in mice

In order to assess the capacity of the synthetic miR-16 to affect prostate tumor growth in mice, we chose to use a mouse model featuring PC-3M-luc cells that have the capacity to form prostate tumors in the bones of mice.[13,15,16] To evaluate that atelocollagen can efficiently deliver synthetic miRNA molecules to metastatic prostate tumors in bone, we generated a PC-3M-luc metastatic prostate cancer cell line stably expressing the renilla luciferase gene fused to the 3′UTR of Bcl2, a validated miR-16 target (**Supplementary Figure S1a**).[17] Thus, this newly engineered cell line PC-3M-Fluc/Rluc-Bcl2 3′UTR expresses both firefly and renilla luciferase, the later of which is under control of miR-16 (**Supplementary Figure S1b**). As expected, transfection of cultured PC-3M-Fluc/Rluc-Bcl2 3′UTR cells with 30 nmol/l of miR-16 deceased the luminescence derived from renilla luciferase (**Supplementary Figure S1c**). To monitor atelocollagen-mediated delivery of miR-16 in the animal, PC-3M-luc/Rluc-Bcl2 3′UTR cells were intracardiac injected into mice and allowed the tumor cells to deposit in the bone. Nine weeks after implantation, the mice were tail-vein injected with 50 μg of miR-16 mimic that was complexed with atelocollagen. Mice injected with the miR-16/atelocollagen complex produced <50% renilla luciferase from tumors in the bone than they produced before treatment (**Figure 2a,b**). The signal from the firefly luciferase that represents tumor growth was unaffected by the synthetic miR-16, indicating that the inhibition observed for renilla luciferase was due to the binding of injected synthetic miR-16 to the 3′UTR of Bcl2. Synthetic miR-16 was detected in tumor tissue at >20 pg/mg tissue when injected systemically and it was observed to persist in tumors for 3 days after injection (data not shown). Thus, our dual-luciferase prostate cancer xenograft model clearly showed that atelocollagen can efficiently deliver active miRNAs into metastatic tumors in mice.

Inhibition of tumor growth in bone tissues in mice with systemic miR-16 treatment

To assess the therapeutic potential of the miR-16/atelcollagen complexes, prostate tumors were initiated in the bones of mice by intracardiac injection of PC-3M-luc cells. A 50 μg of miR-16 mimic complexed with atelocollagen was administered intravenously into mice at 4, 7, and 10 days after prostate tumor initiation (**Supplementary Figure S2**). The development of tumor in the bone was monitored *in vivo* by bioluminescent imaging. At the end of the experiment on day 28, mice treated with the NC miRNA/atelocollagen complex showed the presence of tumor in the thorax, jaws, and/or legs of mice frequently (**Figure 3a**). In contrast, the mice injected with miR-16/atelocollagen complex exhibited no increase in luminescence during the same observation period. There are significant differences between NC and miR-16 treatment groups on day 28 (P < 0.05) (**Figure 3b**). Histopathological analysis also revealed that growth of PC-3M-luc cells in the bone tissues of mice was significantly inhibited by the miR-16 treatment (**Figure 3c**). These data suggest that atelocollagen-mediated systemic delivery of miR-16 could be a novel strategy for inhibition of prostate tumor growth in the bone tissues.

miR-16 expression in human prostate tissues

We used qRT-PCR to quantify miR-16 levels in the tumors and normal adjacent tissues of seven prostate cancer patients as well as four additional prostate tumors. The relative expression level of miR-16 in each of the samples was calculated by comparing to the average normalized miR-16 levels in prostate samples from three normal donors. The average relative expression of miR-16 in the seven prostate normal adjacent samples was 95% with a standard deviation of 16% and the eleven prostate tumors was 73% with a standard deviation of 28% (**Figure 4**). There is a trend toward lower miR-16 expression in prostate tumors versus normal

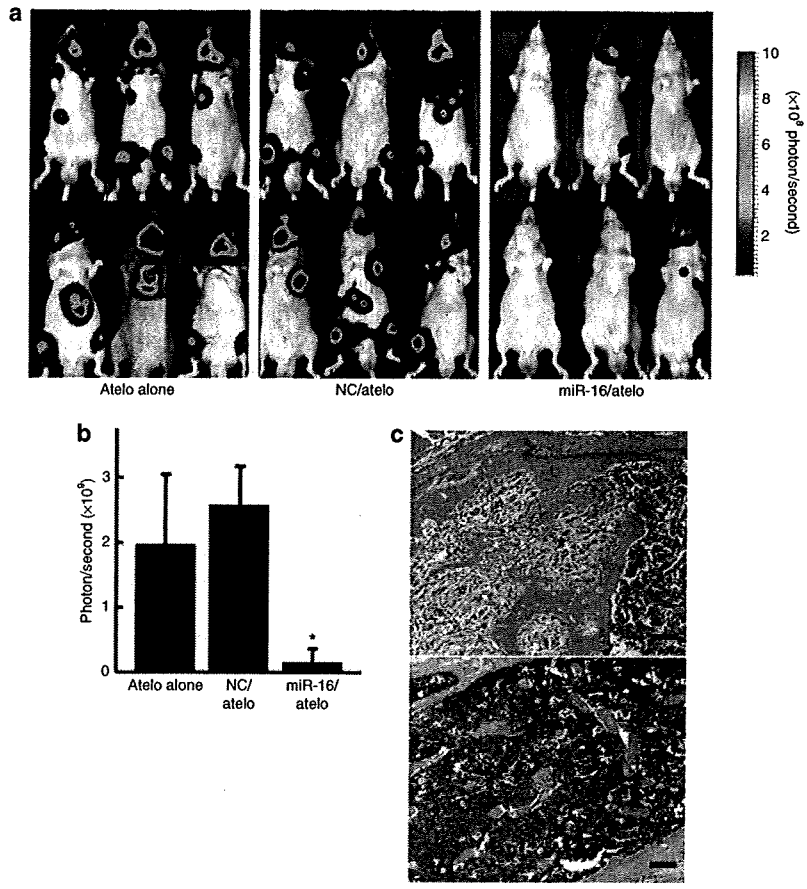

Figure 3 Inhibition of metastatic tumor growth in bone tissues by the atelocollagen-mediated miRNA treatment. Mice were injected with 2×10^6 PC-3M-luc-C6 cells into the left heart ventricle on day zero. The miR-16 and NC miRNA (50 μg) with 0.05% atelocollagen (Atelo) or Atelo alone in a 200 μl volume were injected into the tail vein on days 4, 7, and 10 after tumor injection. At the end of the experiment on day 28, the metastasis was evaluated by IVIS imaging and confirmed by subsequent necropsy. (**a**) All mice used in this experiment on day 28 were shown. There was an increase in luminescence in mice treated with atelocollagen alone and NC miRNA whereas the miR-16/atelocollagen-treated groups had no or low increase in luminescence during the same observation period. (**b**) Quantitation of bioluminescence emitted from whole body of mice on day 28. Data represent the mean (n = 6) ± SD *P<0.05 versus other groups. (**c**) Histopathological analysis confirmed micrometastasis in the tibia of nontreated mice (upper). Metastatic lesions are indicated by asterisk mark. In the miR-16-treated mice, any micrometastasis was not observed (lower). Bar = 100 μm.

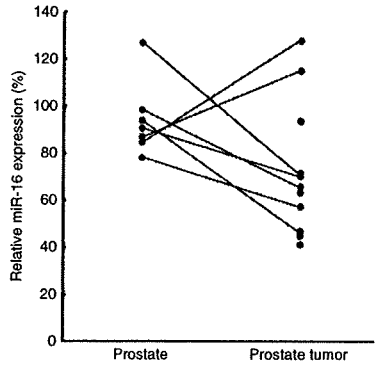

Figure 4 Clinical association of miR-16 expression with prostate cancer. The qRT-PCR analysis to quantify miR-16 levels in the tumors and normal adjacent tissues of seven prostate cancer patients and four additional prostate tumors was performed. The P value calculated by Student's t-test for the two sample sets was 0.08.

prostate tissues, but this trend did not reach statistical significance (**Figure 4**).

mRNA array analysis following transfection of synthetic miR-16

To get insight into the antioncogenic mechanism of miR-16, we transfected PC-3M-luc cells with the miR-16 mimic and analyzed the expressions of mRNA using mRNA array analysis. Exogenously, miR-16 might directly affect the mRNA levels of the target genes and indirectly affect the expression of genes that are downstream of these direct targets.[18] To identify the pathways that could be affected both directly and indirectly by miR-16, total RNA was isolated from the cells 72 hours after miR-16 transfection. The mRNA array data for the miR-16-transfected samples were compared to the NC miRNA–transfected samples (**Supplementary Table S1**). Fold-differential and P value calculations were used to select 285 mRNAs whose expression levels were significantly altered in the miR-16-transfected samples. A selection of genes suppressed

Table 1 Genes suppressed by miR-16

Gene title	Fold-change (miR-16 versus NC)[a]	*P* value[a]	Cellular process[b]
Aurora kinase B	0.61	2.83×10^{-5}	Chromosomal stability
BUB1	0.58	4.34×10^{-8}	Chromosomal stability
BUBR1	0.61	5.73×10^{-6}	Chromosomal stability
Cyclin D3	0.71	1.30×10^{-6}	Cell cycle
CDK1	0.58	4.99×10^{-7}	Cell cycle
CDK2	0.65	2.35×10^{-5}	Cell cycle
Double parked, DUP	0.76	4.07×10^{-5}	Chromosomal stability
Cks1	0.63	4.71×10^{-6}	Cell cycle
Forkhead box M1	0.61	8.19×10^{-6}	Transcription
Polo-like kinase 1	0.72	1.42×10^{-3}	Chromosomal stability
TACC1	0.76	1.56×10^{-4}	Cell cycle
TACC3	0.64	1.51×10^{-5}	Cell cycle
Thymidylate synthetase	0.56	2.50×10^{-8}	Nucleotide synthesis

Abbreviations: miRNA, microRNA; NC, negative control.
[a]Fold change and *P* value were determined by calculating the ratio of global normalized signals from miR-16 transfected cells to NC miRNA–transfected cells in expression array analysis. [b]Genes are clustered by cellular process, according to their gene ontology classification.

Table 2 Classes of genes affected by miR-16

Functional class	Count[a]	%[b]	*P* value[c]
M phase of mitotic cell cycle	20	12.7	9.60×10^{-18}
DNA metabolism	21	13.3	4.00×10^{-7}
Cytoskeleton organization and biogenesis	16	10.1	8.00×10^{-7}
Cytoskeleton-dependent intracellular transport	9	5.7	6.90×10^{-6}
Regulation of progression through cell cycle	15	9.5	2.50×10^{-5}
Mitotic sister chromatid segregation	4	2.5	6.10×10^{-4}
Establishment of cellular localization	13	8.2	4.10×10^{-3}
Mitotic spindle organization and biogenesis	3	1.9	5.50×10^{-3}
Regulation of progression through mitotic cell cycle	3	1.9	8.10×10^{-3}

[a]The number of genes affected in functional pathway. [b]The percentage calculated from the number of genes affected in functional pathway divided by the number of genes included on the arrays. [c]The significance of the appearance of the functional class in affected genes was calculated as *P* value using DAVID 2.0 software.

by miR-16 is listed in **Table 1**. Pathway analysis combining the Kyoto Encyclopedia of Genes and Genomes[19–21] and Database for Annotation, Visualization, and Integrated Discovery[22] was used to analyze the list of genes with altered expression to determine if there was a significant enrichment of genes associated with any known cellular pathways (**Table 2**). Overall, the statistical enrichment of pathways was moderately low, suggesting that no single pathway or network was specifically and vigorously responsive to the treatment. However, for those pathways that were considered enriched, a few strong underlying themes emerged. The gene lists were enriched for functions related to cell division and control of the cell cycle (**Table 2**). The functions associated with cell-cycle control were most enriched in miR-16-affected genes and these 12 genes that cover G1, S, G2, and M phase of cell cycle are mapped into the Kyoto Encyclopedia of Genes and Genomes Pathway Cell Cycle Map (**Supplementary Figure S3**). Thus, these data suggest that strong inhibition of prostate tumor growth in bone tissues of our animal model was due to downregulation of a key component of cell-cycle genes.

DISCUSSION

The likely involvement of miR-16 in the development of prostate cancer is apparent on multiple levels. The loss of the genomic locus at 13q14 that encompasses the miR-16-1 gene has been reported to be highly associated with human prostate cancer progression.[14] Dong *et al.* suggested loss of heterogeneity at 13q14 is associated with clinically significant high-grade and high-stage prostate cancers[10] with ties to both metastasis and tumor initiation.[23] Consistent with its genomic location, our qRT-PCR results showed that the miR-16 is significantly reduced in most prostate tumors and cultured prostate cancer cells relative to normal prostate tissues.

Based on our studies with cultured prostate cancer cells, the reduced expression of miR-16 is likely necessary to maintain high rates of proliferation. The relationship between miR-16 and apoptosis likely stems from the miRNA's apparent role in regulating BCL2 expression.[17] Our previous data also showed that the transfection of miR-16 into 22Rv1 prostate cancer cells induced apoptosis (F. Takeshita *et al.*, unpublished results). Although increased apoptosis is likely to be at least partially responsible for the reduced proliferation rates that we observed in miR-16-transfected PC-3M-luc cells, it appears that the small RNA also affects cell-cycle progression by regulating the expression of multiple cell-cycle genes. The transfection of prostate cancer cells with synthetic miR-16 reduced the expression of genes like *Cyclin D3*, *CDK1*, *CDK2*, *Cks1*, *TAAC1*, and *TAAC3* that play roles in regulating cell-cycle progression. The apparent capacity of miR-16 to simultaneously regulate cell cycle and apoptosis points to the likely importance of the small RNA in maintaining normal cell function and underscores the influence that the altered expression of the miRNA likely has on tumorigenesis.

The importance of miRNAs like miR-16 as tumor suppressors is becoming increasingly clear. Myriad array and qRT-PCR studies have revealed that the expression levels of specific miRNAs are reduced in the tumors of patients with a variety of cancers.[4,5] When transfected into cancer cells, many of these miRNAs affect proliferation, viability, cell cycle, or apoptosis[24,25] and affect the expression of multiple known oncogenes.[17,18,26–28] Although the growth inhibition of LNCaP cells was not induced by transfection of miR-16 in our study, Bonci *et al.* showed that such inhibition of LNCaP cells was induced by transduction of the *miR-15a-miR-16-1* cluster by lentiviral vector.[8] This discrepancy indicated that the growth inhibition of LNCaP might be induced mainly by induction of miR-15a, further careful studies are needed, considering any clinical application of miR-16.

The clinical application of these naturally occurring tumor suppressors represents a major opportunity for the future treatment